iScience

CellPress

Article

# Dynamic $^{13}C$ Flux Analysis Captures the Reorganization of Adipocyte Glucose Metabolism in Response to Insulin

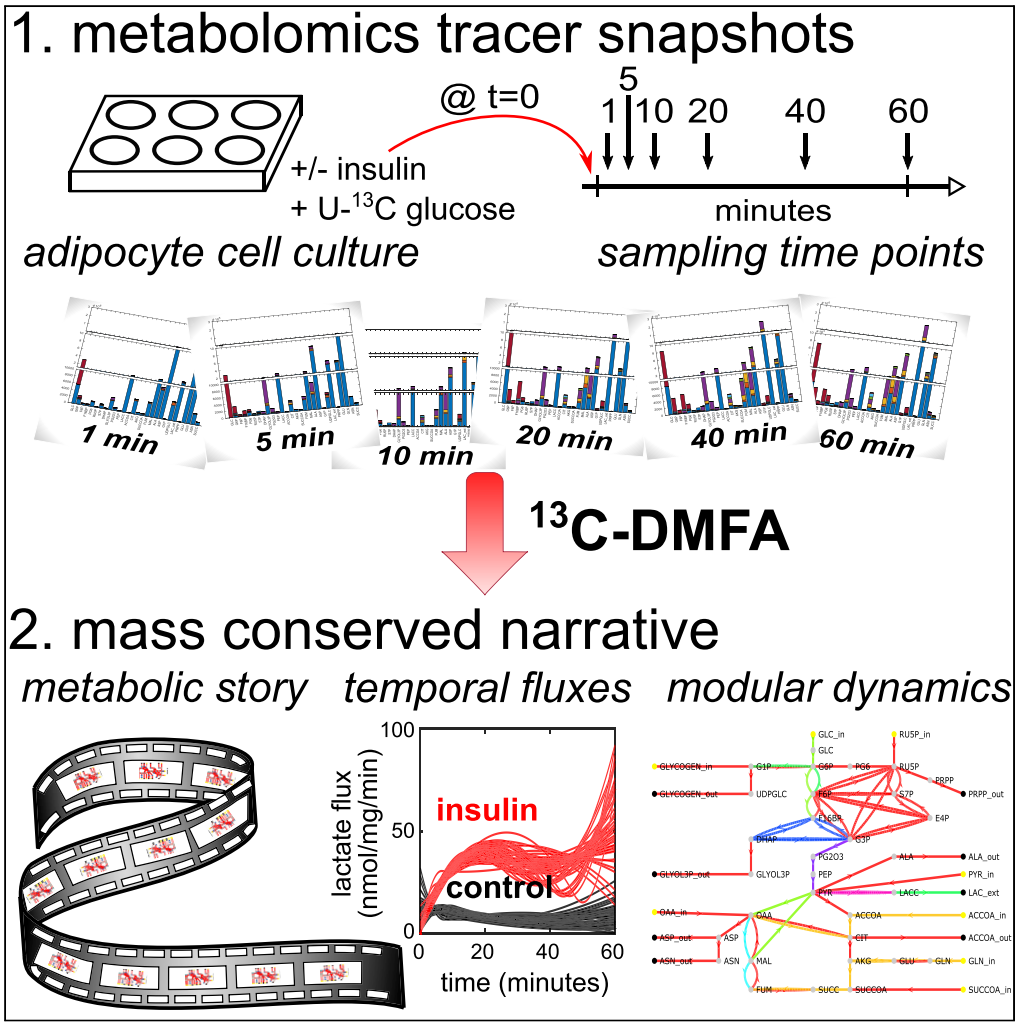


Lake-Ee Quek, James R. Krycer, Satoshi Ohno, ..., Tomoyoshi Soga, David E. James, Shinya Kuroda

lake-ee.quek@sydney.edu.au (L.-E.Q.)
david.james@sydney.edu.au (D.E.J.)
skuroda@bs.s.u-tokyo.ac.jp (S.K.)

## HIGHLIGHTS

An efficient algorithm to solve ODEs generated for large models

Each flux is modeled independently using B-splines

Adipocyte metabolic network showed modular response dynamics

Carbon bookkeeping showed the majority of glucose converted into lactate

Quek et al., iScience *23*, 100855
February 21, 2020 
https://doi.org/10.1016/j.isci.2020.100855

iScience

CellPress

Article

# Dynamic $^{13}C$ Flux Analysis Captures the Reorganization of Adipocyte Glucose Metabolism in Response to Insulin

Lake-Ee Quek,[1,2,14,15,*] James R. Krycer,[1,3,14] Satoshi Ohno,[5] Katsuyuki Yugi,[5,6,10] Daniel J. Fazakerley,[1,3] Richard Scalzo,[11] Sarah D. Elkington,[1,3] Ziwei Dai,[12] Akiyoshi Hirayama,[6,7] Satsuki Ikeda,[6] Futaba Shoji,[6] Kumi Suzuki,[6] Jason W. Locasale,[12] Tomoyoshi Soga,[6,7] David E. James,[1,3,4,13,*] and Shinya Kuroda[5,8,9,13,*]

## SUMMARY

**Cellular metabolism is dynamic, but quantifying non-steady metabolic fluxes by stable isotope tracers presents unique computational challenges. Here, we developed an efficient $^{13}C$-tracer dynamic metabolic flux analysis (13C-DMFA) framework for modeling central carbon fluxes that vary over time. We used B-splines to generalize the flux parameterization system and to improve the stability of the optimization algorithm. As proof of concept, we investigated how 3T3-L1 cultured adipocytes acutely metabolize glucose in response to insulin. Insulin rapidly stimulates glucose uptake, but intracellular pathways responded with differing speeds and magnitudes. Fluxes in lower glycolysis increased faster than those in upper glycolysis. Glycolysis fluxes rose disproportionally larger and faster than the tricarboxylic acid cycle, with lactate a primary glucose end product. The uncovered array of flux dynamics suggests that glucose catabolism is additionally regulated beyond uptake to help shunt glucose into appropriate pathways. This work demonstrates the value of using dynamic intracellular fluxes to understand metabolic function and pathway regulation.**

## INTRODUCTION

Cellular metabolism is dynamic, responding to an ever-changing environment (Kotte et al., 2010; Wegner et al., 2015). The cell's metabolic network is a complex ensemble of fast and slow interacting processes, including feedback mechanisms, but these dynamic behaviors are overlooked in a steady-state step-change experiment (Link et al., 2015) (Figure 1A). Thus we need the ability to quantify metabolic responses over time.

Although metabolomic data are proxy for metabolic responses (Liu and Locasale, 2017), they are not definitive measures of pathway activities (Lee et al., 2017). For instance, when a metabolite decreases, this could be due to reduced synthesis and/or increased degradation (Yugi et al., 2019). Thus, we need to perform flux analysis to quantify the flow of metabolites through metabolic pathways and subsequently reconstruct how the activity of these pathways is altered. This is now commonly accomplished with stable isotope $^{13}C$ tracer experiments because they generate metabolite enrichment data that have quantitative flow information embedded (Cordes and Metallo, 2016; O'Brien et al., 2015). Fluxes that best explain the observed enrichment patterns can be deciphered by modeling, recovering turnover rates and routes of synthesis from isotopically non-stationary metabolite enrichments (Figure 1B).

However, $^{13}C$ flux analysis is challenging because we need to track substrate atoms, often through an intertwining network of reactions in central carbon metabolism (Buescher et al., 2015). Network-level deconvolution by mainstream $^{13}C$ flux analysis packages is largely limited to steady-state metabolism, where fluxes and metabolite levels are constant. More recent software can cater for data sampled from isotopic non-steady state conditions (i.e., metabolism remains constant but with label enrichment increasing over time), but these systems are still studied in a metabolic steady-state (Kogadeeva and Zamboni, 2016; Weitzel et al., 2013; Young, 2014). Techniques like Kinetic Flux Profiling can be used to estimate non-steady fluxes (Alves et al., 2015; Horl et al., 2013; Yuan et al., 2008), but their scope is limited to metabolic pathways with simple label mixing. The current state of the art to infer

[1]Charles Perkins Centre, The University of Sydney, Sydney, NSW 2006, Australia

[2]School of Mathematics and Statistics, The University of Sydney, Sydney, NSW 2006, Australia

[3]School of Life and Environmental Sciences, The University of Sydney, Sydney, NSW 2006, Australia

[4]Sydney Medical School, The University of Sydney, Sydney, NSW 2006, Australia

[5]Department of Biological Sciences, Graduate School of Science, University of Tokyo, Hongo 7-3-1, Bunkyo-ku, Tokyo 113-0033, Japan

[6]Institute for Advanced Biosciences, Keio University, Tsuruoka, Yamagata 997-0052, Japan

[7]AMED-CREST, AMED, 1-7-1 Otemachi, Chiyoda-Ku, Tokyo 100-0004, Japan

[8]Department of Computational Biology and Medical Sciences, Graduate School of Frontier Sciences, University of Tokyo, 5-1-5 Kashiwanoha, Kashiwa, Chiba 277-8562, Japan

[9]CREST, Japan Science and Technology Agency, Bunkyo-ku, Tokyo 113-0033, Japan

[10]YCI Laboratory for Trans-Omics, Young Chief Investigator Program, RIKEN Center for Integrative Medical Sciences, 1-7-22 Suehiro-cho, Tsurumi-ku, Yokohama, Kanagawa 230-0045 Japan

[11]Faculty of Engineering and Information Technologies, The University of Sydney, Sydney, NSW 2006, Australia

*Continued*

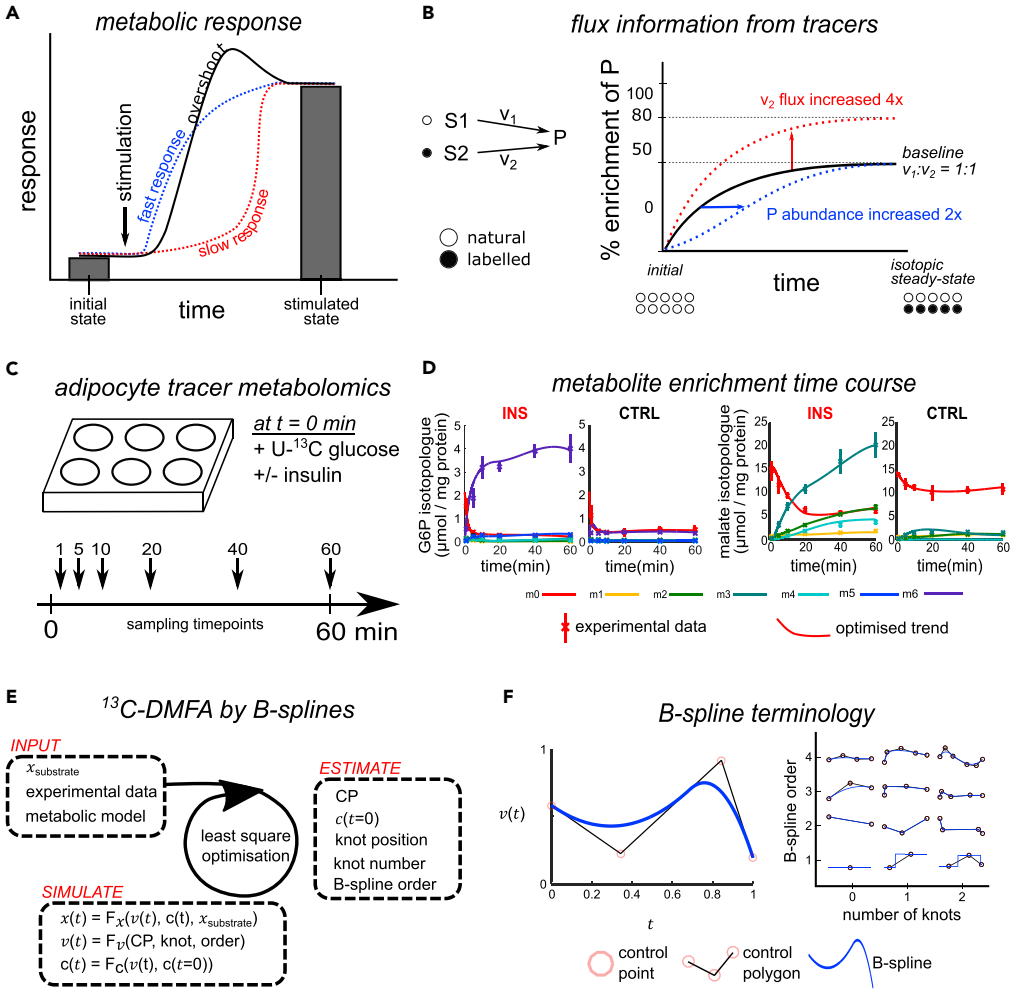


**Figure 1. 13C-DFMA Performed Using B-Splines to Investigate Acute Insulin Metabolic Response**

(A) Trajectories of metabolic response and information missed by steady-state measurements.

(B) The trajectory of metabolite P enrichment is a measure of pathway flux contribution and turnover rate. P is produced from unlabeled S1 and labeled S2. Relative to baseline (black), increasing $v_2$ flux (red) increases the speed and amount of P enrichment. Increasing P abundance (blue) reduces the speed of P enrichment.

(C) 3T3-L1 adipocyte tracer experiment showing simultaneous addition of insulin and uniformly labeled glucose and the subsequent sampling time points.

(D) Examples of metabolomics data collected, isotopologues of glucose 6-phosphate (G6P), and malate. Optimized solutions shown as trend lines. Data are represented as mean ±2×SEM of 3 biological replicates.

(E) The optimization strategy used in 13C-DMFA to solve the inverse problem by iterative simulation of isotopologues by estimating system's parameters.

(F) The shape of B-splines is manipulated by controlling the coordinates of the control points (CP). More complex curves have more CPs and are produced by increasing knots and order.

See also Figure S1.

network-level non-steady fluxes from $^{13}C$ enrichment data is to use linear piecewise affine approximations of fluxes (PWA) (Abate et al., 2012; Schumacher and Wahl, 2015).

To model curves, PWA's workflow first breaks time-dependent fluxes into linear pieces; then the fluxes are estimated in segments. The first task of optimizing the number and the placement of these breakpoints uses only metabolite abundances, but not enrichments (Schumacher and Wahl, 2015), as currently there is no elegant way to use both. This is not ideal because, in balanced flux scenarios, the metabolite levels will appear constant despite the underlying fluxes being dynamic (Figures S1A–S1D). When optimized

[12]Department of Pharmacology and Cancer Biology, Duke University School of Medicine, Duke University, Durham, NC 27710, USA

[13]Senior author

[14]These authors contributed equally

[15]Lead Contact

*Correspondence: lake-ee.quek@sydney.edu.au (L.-E.Q.), david.james@sydney.edu.au (D.E.J.), skuroda@bs.s.u-tokyo.ac.jp (S.K.)

https://doi.org/10.1016/j.isci.2020.100855

breakpoints are too sparse to capture the underlying curvature, the latter flux estimation will struggle to produce a good fit.

Fluxes are estimated by least-square optimization (Wiechert et al., 2001), but this task is computationally intensive when dealing with a regular-sized central carbon metabolism model. The tracking of tracer atom propagations involves solving isotope balance equations. These ordinary differential equations (ODE) form a stiff problem owing to the coexistence of very slow and very fast reactions. Implementing non-steady fluxes worsens the situation because metabolite pool sizes are changing at different paces as well. Any task that involves running optimization repeatedly becomes overwhelmingly slow, such as model and data troubleshooting and sensitivity analyses by resampling. Thus, we aimed to make non-steady-state metabolic flux analysis of stable isotope tracer data more generalized and implementable.

Here, we present a generalized computational framework for performing $^{13}C$ dynamic metabolic flux analysis (13C-DMFA). The crux of our solution was using B-splines to model time-dependent fluxes (Martínez et al., 2015), analogous to drawing curves in vector-based graphics. B-splines made it possible to (1) use higher-order curves to reconstruct a variety of flux trajectories and (2) apply a more stable algorithm to speed up flux estimation.

As a proof of principle, 13C-DMFA was applied to characterize how cultured adipocytes process glucose in response to insulin, which stimulates protein phosphorylation within seconds and glucose uptake within minutes (Humphrey et al., 2013; Krycer et al., 2017). We found that flux rates varied substantially between pathways, responding to insulin with differing speeds and to differing magnitudes. The modular organization-portrayed pathway flux dynamics suggests that glucose catabolism was not simply an autonomous cascade driven by glucose influx. Overall, this work provides a MATLAB-based package and a workflow to perform $^{13}C$-tracer flux analysis on non-steady-state systems.

## RESULTS

### Network-Level Modeling Is Required to Extract Dynamic Flux Information

We previously examined how the adipocyte metabolome changed in response to acute insulin treatment (Krycer et al., 2017). We used 3T3-L1 cells (Green and Kehinde, 1975), a mouse embryonic fibroblast cell line that was differentiated into adipocytes before treatment. Briefly, 3T3-L1 adipocytes were exchanged to media containing uniformly labeled $^{13}C_6$-glucose and immediately treated with or without insulin (INS and CTRL, respectively) (Figure 1C). Lactate in the media and 27 intracellular metabolites were then measured at six time points (1, 5, 10, 20, 40, and 60 min) after treatment by mass spectrometry (capillary electrophoresis-time of flight and electrospray ionization-tandem mass spectrometry) and then normalized to protein content (units: pmol/mg protein). It was obvious that insulin altered pathway fluxes, if not, metabolite abundances (Figure 1D). Insulin increased glucose uptake rapidly, and glucose propagated into various metabolic pathways at different speeds (Krycer et al., 2017). This was assessed by examining the levels and $^{13}C$-enrichment of individual metabolites, treating them as separate entities.

Here, we sought to apply network-level flux modeling to understand how adipocytes process glucose in response to insulin. Enrichment states of the metabolites were increasing in a cascading manner, with distal metabolites like tricarboxylic acid (TCA) cycle intermediates enriching slower than metabolites proximal to glucose uptake. The lag observed in the metabolite enrichments is intricately linked to how metabolic fluxes are changing with insulin stimulation and how the metabolites are connected. Thus we applied mass conservation principles, namely, via metabolite balance equations and isotopologue balance equations (Antoniewicz et al., 2007; Quek et al., 2010), to infer these fluxes by modeling the transfer of carbon atoms between metabolites. As the steady-state assumption is no longer valid, this raised the challenge of estimating time-dependent fluxes by optimization, which we address in the following sections.

### Non-steady Fluxes and Near-Zero Isotopologues Make the 13C-DMFA Problem Hard to Optimize

Generalizing for a network of reactions, the isotopologues of metabolites over time $X(t)$ can be expressed as a function of the metabolic fluxes $v(t)$ and the system's boundary conditions, namely, the initial metabolite concentrations $c(t=0)$ and the enrichment of input substrates $X_{substrate}$. $X(t)$ is often expressed in the intensive form $x(t)=X(t)/c(t)$ as isotopologue fractions; note that $\sum X_q = c_q$ and $\sum x = 1$. This forward problem is a system of non-linear ODEs (Dai and Locasale, 2017), which means the inverse problem of

estimating $v(t)$ from $x(t)$ is solved by least-square optimization (Figure 1E). Mainstream techniques are limited to constant $v(t)$ and $x(t)$, i.e., steady-state metabolism (Buescher et al., 2015; Wiechert and de Graaf, 1997), due to the computational difficulties faced when optimizing non-steady fluxes.

The crux of dynamic flux analysis is to parameterize each $v(t)$ independently, but this creates computational issues during the optimization. When a metabolite's total influx and efflux are not equal (i.e., imbalanced), the metabolite's concentration and isotopologue abundance will increase (influx > efflux) or decrease (influx < efflux). The allowance for imbalanced fluxes significantly increases the encounter of infeasible points where $c(t)<0$ and $x(t)<0$ during optimization, especially when effluxes can exceed influxes. Core to this problem is that numerically ensuring $c(t)>0$ does not guarantee $x(t)>0$, as the latter is estimated numerically with smaller steps.

The risk of encountering negative is ever present despite having established $c(t)>0$ numerically, because (1) most $x(t)$ are trending toward or away from zero in a pulse tracer experiment, (2) the initial guesses for optimization are almost always infeasible, and (3) underdetermined parameters often settle just within the feasible envelope. Negative $c(t)$ and $x(t)$ are not caused by numerical or truncation errors; in an iterative method they are still mathematically valid outputs of $v(t)$ because efflux exceeding influx can lead to a deficit. However, as $x(t)$ is an intensive variable, adaptive ODE solvers cannot progress past the point of reaching negative $x(t)$ due to subsequent numerical instability, causing the solver to take even smaller steps.

Currently there is no way to avoid breaching the feasible envelope when ODE solvers are used during optimization. In particular, infeasible points are difficult to anticipate numerically because negative values may only emerge when smaller steps are taken (Figure 2A). The abrupt stalling of ODE solvers causes optimizations to terminate prematurely, which occurs more frequently with larger models. Thus, we considered B-splines as an alternative, to efficiently (1) contain the optimization in the feasible space and (2) guarantee $x(t)$ is positive when evaluated in the feasible space.

## B-Splines Provide Means to Keep Optimization in the Feasible Space

Briefly, B-splines are piecewise polynomial functions that can be expressed as basis functions (Figure 1F). They can be used to draw any curve, directly addressing our need to parameterize time-dependent flux trajectories in a generalized manner. B-spline computation is fast because the system can be rendered linear, enabling the use of matrix algebra.

Here, time-dependent trajectories of fluxes $v(t)$ and metabolites $c(t)$ are expressed as a linear combination of B-spline basis functions $N$ and $\int N$, respectively (Equations 1 and 2). $N$ and $\int N$ are coefficient matrices generated by the Cox-de Boor recursion formulation, using a prescribed set of time steps, knot positions, and order of splines (e.g., 1 = constant; 2 = linear; 3 = quadratic) (Figures S1E–S1H) (Martínez et al., 2015; Vercammen et al., 2014). Using the stoichiometric matrix $S$, a matrix representation of the metabolite balance equations (Quek et al., 2010), $c(t)$ is calculated analytically by integrating $v(t)$, given the initial metabolite concentrations $c_0$. The B-spline construction and integration are further elaborated in Transparent Methods.

$$\underbrace{v(t)}_{\substack{\text{flux trajectory}\\ R \times T}} = \underbrace{CP}_{\substack{\text{control points}\\ R \times j}} \cdot \underbrace{N}_{\substack{\text{coefficient matrix}\\ j \times T}} \qquad \text{Equation 1}$$

$$\underbrace{c(t)}_{\substack{\text{metabolite trajectory}\\ M \times T}} = S \int v(t)dt$$

$$= \underbrace{S}_{\substack{\text{stoic. matrix}\\ M \times R}} \cdot \underbrace{[0 \quad CP]}_{\substack{\text{control points}\\ R \times (j+1)}} \cdot \underbrace{\int N}_{\substack{\text{coefficient matrix}\\ (j+1) \times T}} + \underbrace{c_0}_{\substack{\text{initial conc.}\\ M \times T}} \qquad \text{Equation 2}$$

for $R$ reactions, $M$ metabolites, $T$ time steps, and $j$ = (order + number of internal knots).

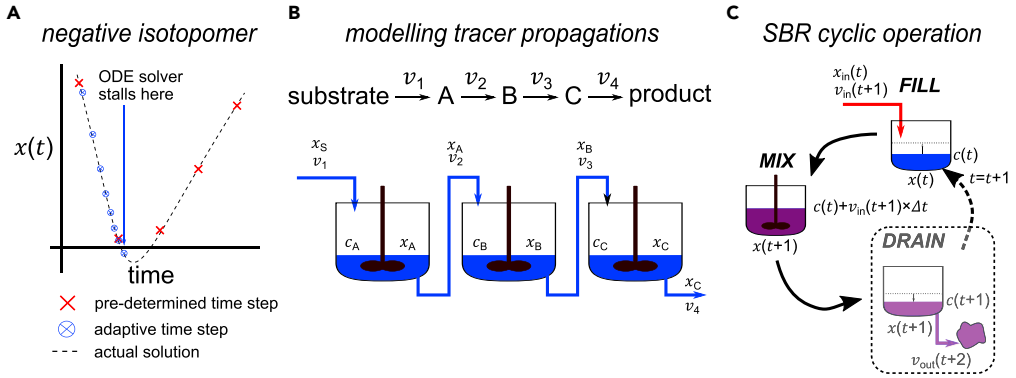


D

SBR scheduling

| time step | SBR mode | A | | | | B | | | | C | | | |
|---|---|---|---|---|---|---|---|---|---|---|---|---|---|
| | | $x$state | $c$state | $v_{in}$ | $v_{out}$ | $x$state | $c$state | $v_{in}$ | $v_{out}$ | $x$state | $c$state | $v_{in}$ | $v_{out}$ |
| | START | $x_A(t_0)$ | $c_A(t_0)$ | - | $v_2(t_1)$ | $x_B(t_0)$ | $c_B(t_0)$ | - | $v_3(t_1)$ | $x_C(t_0)$ | $c_C(t_0)$ | - | $v_4(t_1)$ |
| 0 | fill | $x_A(t_0)$ | $c_A(t_0)$ | $v_1(t_1)$ | - | $x_B(t_0)$ | $c_B(t_0)$ | $v_2(t_1)$ | - | $x_C(t_0)$ | $c_C(t_0)$ | $v_3(t_1)$ | - |
| | mix | $x_A(t_1)$ | $c_A(t_0)+v_1(t_1)\Delta t$ | - | - | $x_B(t_1)$ | $c_B(t_0)+v_2(t_1)\Delta t$ | - | - | $x_C(t_1)$ | $c_C(t_0)+v_3(t_1)\Delta t$ | - | - |
| | drain | $x_A(t_1)$ | $c_A(t_1)$ | - | $v_2(t_2)$ | $x_B(t_1)$ | $c_B(t_1)$ | - | $v_3(t_2)$ | $x_C(t_1)$ | $c_C(t_1)$ | - | $v_4(t_2)$ |
| 1 | fill | $x_A(t_1)$ | $c_A(t_1)$ | $v_1(t_2)$ | - | $x_B(t_1)$ | $c_B(t_1)$ | $v_2(t_2)$ | - | $x_C(t_1)$ | $c_C(t_1)$ | $v_3(t_2)$ | - |
| | mix | $x_A(t_2)$ | $c_A(t_1)+v_1(t_2)\Delta t$ | - | - | $x_B(t_2)$ | $c_B(t_1)+v_2(t_2)\Delta t$ | - | - | $x_C(t_2)$ | $c_C(t_1)+v_3(t_2)\Delta t$ | - | - |
| | drain | $x_A(t_2)$ | $c_A(t_2)$ | - | $v_2(t_3)$ | $x_B(t_2)$ | $c_B(t_2)$ | - | $v_3(t_3)$ | $x_C(t_2)$ | $c_C(t_2)$ | - | $v_4(t_3)$ |
| 2 | fill | $x_A(t_2)$ | $c_A(t_2)$ | $v_1(t_3)$ | - | $x_B(t_2)$ | $c_B(t_2)$ | $v_2(t_3)$ | - | $x_C(t_2)$ | $c_C(t_2)$ | $v_3(t_3)$ | - |
| | mix | $x_A(t_3)$ | $c_A(t_2)+v_1(t_3)\Delta t$ | - | - | $x_B(t_3)$ | $c_B(t_2)+v_2(t_3)\Delta t$ | - | - | $x_C(t_3)$ | $c_C(t_2)+v_3(t_3)\Delta t$ | - | - |
| | drain | $x_A(t_3)$ | $c_A(t_3)$ | - | $v_2(t_4)$ | $x_B(t_3)$ | $c_B(t_3)$ | - | $v_3(t_4)$ | $x_C(t_3)$ | $c_C(t_3)$ | - | $v_4(t_4)$ |
| | | | | | | | | | | | | | |
| $t$ | fill | $x_A(t)$ | $c_A(t)$ | $v_1(t+1)$ | - | $x_B(t)$ | $c_B(t)$ | $v_2(t+1)$ | - | $x_C(t)$ | $c_C(t)$ | $v_3(t+1)$ | - |
| | mix | $x_A(t+1)$ | $c_A(t)+v_1(t+1)\Delta t$ | - | - | $x_B(t+1)$ | $c_B(t)+v_2(t+1)\Delta t$ | - | - | $x_C(t+1)$ | $c_C(t)+v_3(t+1)\Delta t$ | - | - |
| | drain | $x_A(t+1)$ | $c_A(t+1)$ | - | $v_2(t+2)$ | $x_B(t+1)$ | $c_B(t+1)$ | - | $v_3(t+2)$ | $x_C(t+1)$ | $c_C(t+1)$ | - | $v_4(t+2)$ |

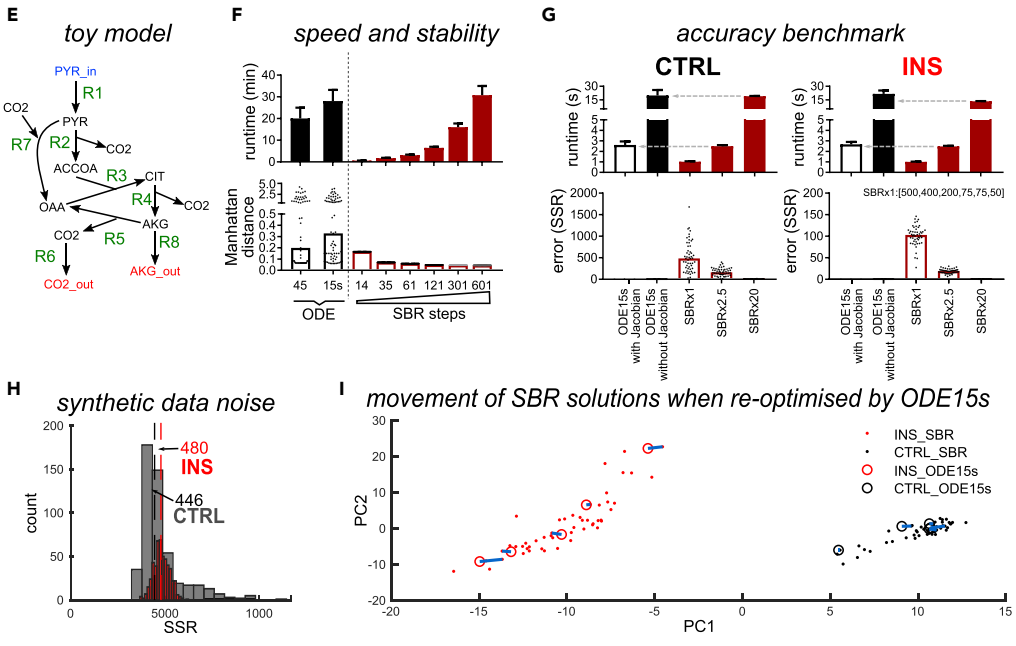


**Figure 2. The SBR Algorithm Overcomes Stability Issue Encountered by Conventional ODE Solvers**

(A) As SBR utilizes predetermined time steps, negative isotopologues are avoided when $x(t)$ is evaluated at the given time steps, even though negative values are part of the true solution. ODE solvers are unable to forecast the infeasibility because time steps are determined dynamically.

(B) Isotopologue propagation in a metabolic network is abstracted as a series of tanks and modeled by mass conservation equations.

(C) Schematic of the Sequencing Batch Reactors (SBR) algorithm. Each tank follows the cyclic sequence of fill, mix, and drain. The drain step is not computed by the SBR algorithm.

(D) The schedule of the sequence shows that the "drain" step can be omitted because $x(t+1)$ is an intensive value calculated during the "mix" step.

**Figure 2. *Continued***

(E) The toy TCA cycle model used to test performance of the SBR algorithm.

(F) SBR is generally faster and converges more consistently at the theoretical solution than MATLAB's ODE45 and ODE15s solvers. Manhattan distances are used to measure deviations from the true solution, with bars showing median values. Error bars show interquartile range of 100 replicates.

(G) Benchmarking SBR's speed-accuracy trade-off at the scale of a real (i.e., adipocyte) model. EMUs generated by SBR are as accurate as ODE solvers', but will require as much computational time as ODE15s without the Jacobian, which is slower than with the Jacobian. SSRs measure the weighted deviations of EMUs from the "true" measurements generated by ODE15s (with Jacobian) using prototyping CTRL and INS solutions. Bars show median values. SBRx2.5 and SBRx20 refer to increasing SBR's number of steps by 2.5- and 20-fold relative to the optimized SBR time steps showed in Figure 3D (SBRx1). Error bars show interquartile range of 100 replicates.

(H) The expected error in the CTRL and INS datasets when corrupted randomly with one standard deviation noise.

(I) When optimized again using ODE15, five randomly chosen CTRL and INS solutions generated by SBR did not change significantly relative to the rest of the SBR solutions.

Equations 1 and 2 show that we can control $v(t)$ using just one very simple system of parameterization: the number of control points (CP) and their XY-coordinates and order of the B-spline (Figure S1G). This system resembles how we construct B-splines in graphic software. Note the number of knots is the number of CP minus the B-spline order; $c(t)$ is determined from $v(t)$ and $c_0$ (Equation 2). With reference to PWA, knots are equivalent to breakpoints, the order is 2 (i.e., linear), and the formulation for $v(t)$ and $c(t)$ are exactly the same. The main difference is that to model flux trajectories with greater curvature, the order of B-splines can be increased as well instead of just the number of knots/breakpoints.

Most importantly, once the knot sequence and order of splines are prescribed, $v(t)$ and $c(t)$ are linear with respect to the estimated parameters $CP$. This circumvents solving $c(t)$ numerically, thus allowing the incorporation of $c(t)>0$ as linear constraints to define the feasible bounds for optimization.

## Euler Method Improvised to Eliminate Negative Isotopologues

Next, we sought to eliminate negative isotopologues $x(t)<0$. To achieve this, first we will describe how $X(t)$ is calculated. Cell metabolism can be abstracted as a network of continuous stirred tank reactors, with the contents of a tank and the flow between tanks representing the metabolite pool and their inter-conversion, respectively (Figure 2B) (Cordes and Metallo, 2016). This abstraction can be dissected further at the sub-molecular level, treating atoms or group of atoms of metabolites as separate tanks, for instance, to deal with cleavage reactions.

This is accomplished by the Elementary Metabolite Unit (EMU) framework (Antoniewicz et al., 2007). Within this framework, $X(t)$ denotes isotopologue abundances at time $t$. An EMU of a metabolite is a distinct group of the metabolite's atoms. For example, three-carbon pyruvate can be decomposed into seven EMUs sized from 1 to 3 ($PYR_1$, $PYR_2$, $PYR_3$, $PYR_{12}$, $PYR_{23}$, $PYR_{13}$ and $PYR_{123}$, where $PYR_x$ denotes carbon $X$ as a member of that particular EMU). The propagation of $^{13}C$ atoms through a network of isotopologues can be tracked by mass conservation. Equation 3 represents a generalized form of the EMU balance equation, with $X$ and $x$ now representing EMUs and their fractions. The EMU framework is elegant because it invokes the least number of balancing equations and is compatible with mass spectrometry data.

$$\underbrace{\frac{dX_q}{dt}}_{EMU\ balance} = \frac{d(c \bullet x)_q}{dt} = \underbrace{\sum (v_{in} \bullet x_{in})}_{EMU\ in} - \underbrace{x_q \bullet \sum v_{out}}_{EMU\ out} \text{ for metabolite } q \qquad \text{Equation 3}$$

where $\sum X_q = c_q$ and $\sum x = 1$

Equation 3 is often solved numerically using ODE solvers. The forward Euler Method (Equation 4) is the simplest numerical approach but is sufficient to demonstrate that $X_{q,\ t+1}$ can become negative when the EMU efflux term is too large. $X_{q,\ t+1}<0$ is difficult to avoid numerically because adaptive solvers reduce the step size dynamically to suppress numerical error, but the sudden occurrence of negative $X(t)$ would destabilize the equation system and amplify numerical error as a result. This causes the ODE solver to take even smaller steps, until the solver stalls completely because negative $X(t)$ is indeed the solution. In our hands, rounding negative values up to zero did not improve convergence rate of optimization. In contrast, B-splines uses predetermined time steps and are not adjusted dynamically.

$$X_{q,\,t+1} = X_{q,\,t} + \underbrace{\Delta t \cdot \sum (v_{in,t} \cdot x_{in,t})}_{influx} - \underbrace{\Delta t \cdot x_{q,t} \cdot \sum v_{out,t}}_{efflux} \quad \text{Equation 4}$$

To eliminate the negative term altogether, we simply treated metabolite conversions as "sequencing batch reactors" (SBR) (Figure 2C). The operation of SBR is composed of three stages, namely fill, mix, and drain, cycled repeatedly in discrete steps to model the continuous conversion of metabolites over time (Figure 2D). In each step, the SBR algorithm cycles through the three stages, first accounting for the bolus addition of new metabolites to the existing pool (fill), followed by mixing of the new and existing metabolites (mix), and finally reducing the post-mix pool to produce the existing pool for the next cycle (drain). The "mixing" equation sums the normalized EMU contributions of source substrates ($v_{in,t+1} \cdot \chi_{in,t}$) and the existing pool ($c_{q,t} \cdot \chi_{q,t}$) at a given time step $t$ (Equation 5). Note that $x_{t+1}$ is an intensive variable carried over to the next cycle and is calculated before the "drain" step.

$$x_{q,t+1} = \frac{X_{q,t+1}^{post-mix}}{\underbrace{\Delta t \cdot \sum v_{in,t+1} + c_{q,t}}_{mixing\ volume}} = \frac{X_{q,t+1}^{post-mix}}{\sum X_{q,t+1}^{post-mix}} \quad \text{for metabolite } q \text{ at time } t, \text{ where} \quad \text{Equation 5}$$

$$X_{q,t+1}^{post-mix} = \overbrace{\Delta t \cdot \sum (v_{in,t+1} \cdot x_{in,t})}^{new\ metabolites} + \overbrace{c_{q,t} \cdot x_{q,t}}^{existing\ pool}$$

The discretization in SBR takes advantage of how B-splines are calculated using predetermined time steps. With the efflux term absent in Equation 5, $x_{t+1}$ is always positive when Equation 5 is evaluated at time steps satisfying the constraint $c_t>0$. Thus we circumvented negative values during optimization as long as $c_t$ are positive at the time steps taken (Equation 2), even if solutions for $c(t)$ or $x(t)$ include negative values. Despite eliminating the efflux term, mass conservation is still enforced because the size of the existing pool $c_{q,t}$ is calculated analytically with respect to $v(t)$ by B-spline integration.

## The SBR Algorithm Is Fast, Accurate, and Numerically Stable

The SBR approach was benchmarked against ODE optimization using an eight-reaction toy model representing the citric acid cycle (TCA) (Figure 2E, see Transparent Methods). Optimization solutions were generated by solving Equation 3 using MATLAB's *ODE45* and *ODE15s*, and by the SBR approach using Equation 5. All methods converged at the theoretical solution. The Manhattan distance between the optimized values and the theoretical solution showed that SBR excelled by consistently converging at the optimum, whereas ODE solvers suffered failure rates of at least 60% (Figure 2F). The inability of the ODE solvers to converge consistently at this toy scale, indicated by a large spread in the calculated Manhattan distances when compared with the SBR approach, demonstrated potential optimization challenges for real models.

SBR time steps with decreasing sizes were tested to evaluate the trade-off between the numerical accuracy of calculating $x(t)$ and runtime. For an SBR approach to be as accurate as ODE45, 35 steps were required, but computation was still 10-fold faster based on the median runtime of optimizations that converged (Figure 2F).

The above-mentioned results indicated that we have a good margin for calibrating SBR time steps such that high/comparable computational accuracy is obtained without being slower than ODE solvers. We next made a similar comparison, using INS and CTRL datasets. We found that to achieve the same level of accuracy as ODE solvers, the SBR algorithm took as long as the ODE15s without the Jacobian (Figure 2G). Matching the time taken by ODE15s with Jacobian, which was as accurate but 7- to 10-fold faster than ODE15s without the Jacobian, increased SBR errors (Figure 2G), but they were still within the tolerance of noisy data (error <500, Figure 2H). As expected, the numerical errors incurred for CTRL were greater than for INS because SBR time steps were calibrated using INS dataset. We struggled to complete the optimizations when we used ODE solvers, but we showed that re-optimizing SBR solutions using ODE15s with Jacobian neither shifted the SBR solutions significantly nor improved the fit (Figure 2I). Thus the performance of the SBR algorithm is at least on par with ODE solvers, but is significantly more stable.

### Using the Adipocyte Data to Design a Practical 13C-DMFA Workflow

Another advantage of the SBR approach is that it makes our workflow highly amenable to prototyping, the iterative process of testing model-to-data fit followed by *ad hoc* modifications (Figure 3A). This takes advantage of the ease to manipulate optimizations for speed over accuracy to achieve quicker learning cycles to improve the model. For prototyping, the SBR time steps taken were coarse and arbitrary, 20 uniform steps between sampling time points.

The optimization objection function (Equation 6) was defined based on isotopologue concentrations for 27 intracellular metabolites and extracellular lactate over time and the incorporation of radiolabeled $^{14}$C-glucose into glycogen and fatty acids at 60 min (Data S1). The construction and components of Equation 6 are described in greater detail in Figure S2A and Transparent Methods. The optimization procedure implemented largely adhered to existing 13C-MFA methodologies (Quek et al., 2009) (see Transparent Methods, Data S4). Briefly, *CP* and $c_0$ (from Equation 2) were estimated by minimizing the sum of squared residuals (SSR) calculated by the objective function (Equation 6), using MATLAB's constrained non-linear solver *fmincon*. Residual errors between the measured ($data_{exp}$) and simulated ($data_{sim}$) were weighted by the respective measurement errors (*error weight*). The objective function was scripted dynamically to accommodate frequent changes during prototyping, as well as to deal with missing values and gaps in the metabolite data (Figure S2B).

$$\min(SSR) = \min_{\begin{bmatrix} CP \\ c_0 \end{bmatrix}} \sum \left( \frac{data_{exp} - data_{sim}}{error\ weight} \right)^2 \qquad \text{Equation 6}$$

subjected to $c(t)>0$, $v(t)\geq 0$

We used the adipocyte metabolite data to dictate the reconstruction of the central carbon model (Figures 3B and 4A, see Transparent Methods). Reaction pathways were assembled such that metabolites showing significant enrichment were traceable to glucose. Redundant or alternative routes were included at first, and subsequently marginalized by examining the fit of the candidate model against the adipocyte data (results not shown). For example, lactate had m+3 and m+2 label, but there was a lack of substantial m+3 and m+2 labeling for glucose 6-phosphate (G6P) and phosphoenolpyruvate (PEP) respectively, suggesting that gluconeogenic (or glyceroneogenic) flux was not significant relative to glycolysis; thus we eliminated PEP carboxykinase. In addition, the high m+3 label in malate indicated that pyruvate anapleurosis should be included. A single compartment model was adopted because, for adipocytes, metabolites are largely synthesized or consumed in a single compartment. There is a general lack of parallel pathways that can give rise to compartment-specific enrichment profiles. For example, as glucose and branched-chain amino acids are the major substrates for *de novo* lipogenesis (Green et al., 2016), and reductive carboxylation is negligible in adipocytes (Koh et al., 2004; Liu et al., 2016), the cytosolic synthesis of citrate from oxoglutarate was omitted. Furthermore, due to the lack of compartment-specific metabolite data, it was more conservative to use a single-compartment model to avoid overfitting. The availability of compartment-specific metabolite data in the future would enable the modeling of additional pathways such as the malate-aspartate shuttle, which likely operates in our cell system but could not be resolved by our tracer dataset.

We also considered metabolic inputs and outputs to the reaction network, which are important to consolidate the metabolite data (Figure 3B). The former causes dilution of label at specific points of the network, and the latter draws carbon out of the system to create flow through a pathway. Major inputs (glycolysis, glutamine anapleurosis) and outputs (lactate production, aspartate catapleurosis) were specified upfront, then minor inputs and outputs were deduced from the data, either by inspection of the data or by modeling trial and error. For example, pyruvate and AcCoA influxes were found to be essential to create entry of unlabeled substrates upstream of the TCA cycle in the CTRL dataset (Data S1). Unlabeled pyruvate can be produced by alanine transaminase, and AcCoA, by fatty acid oxidation in the mitochondria.

The final adipocyte metabolic model used for flux estimation contained 66 reactions and 34 internal metabolites; the same model was used for both INS and CTRL datasets to facilitate comparison (Data S1). Initially, the model could not recapitulate the unlabeled (m0) fractions, which were unexpectedly high and stable (Figure S3A). Thus, nuisance parameters were introduced *ad hoc* to represent "stagnant" partitions (Antoniewicz, 2018), which improved data fitting significantly as shown by a reduction in Akaike information criterion (AIC) (Figure S3B).

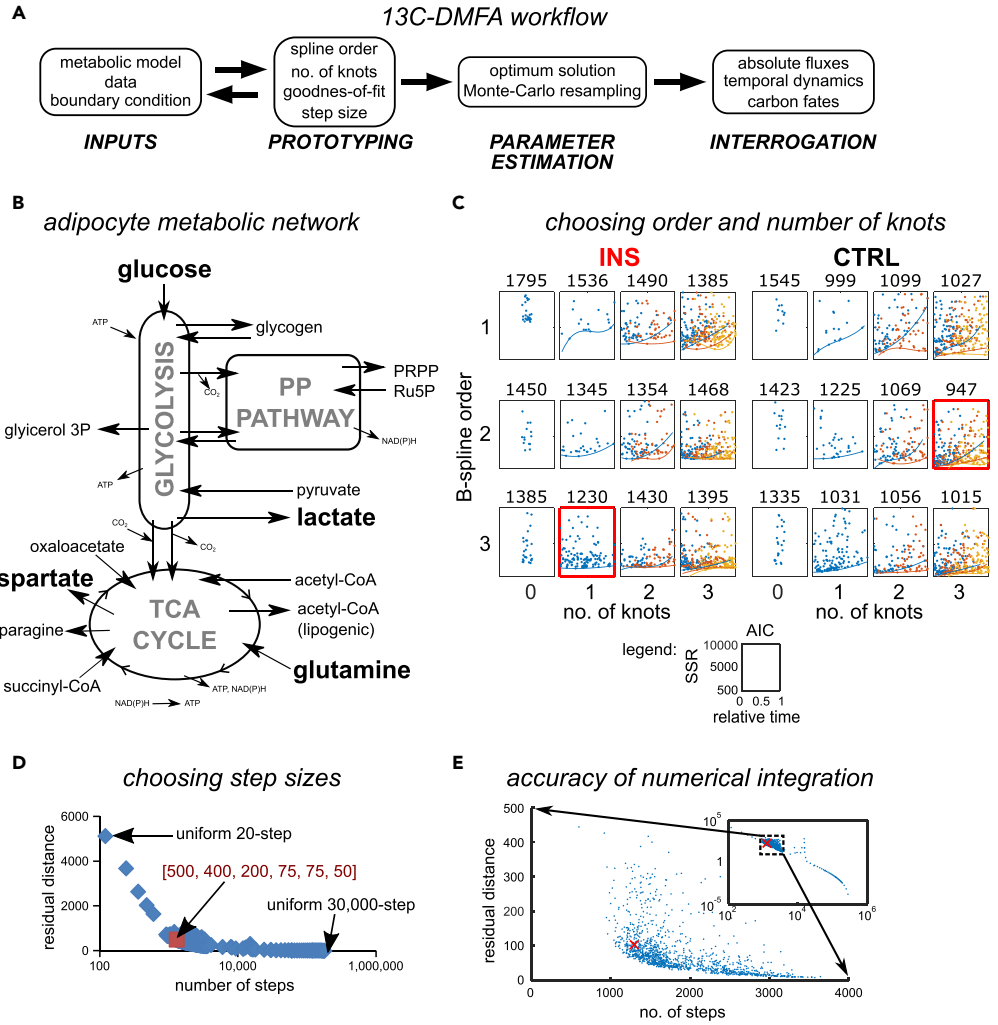


**Figure 3. A 13C-DMFA Workflow that Incorporates a Prototyping Phase to Improve Model Fit**

(A) Overview of the 13C-DMFA workflow, showing iterative input revision and prototyping, followed by optimization and results interrogation.

(B) An abridged diagram of adipocytes central metabolism showing placement of key inputs and outputs.

(C) AIC was used to help choose the B-spline orders and number of knots used for parameter estimation chosen based on the lowest AIC for INS. Placement of the first (blue), second (red), and third (orange) knots shown, with correspondingly colored cubic curves marking knots' lower envelope.

(D) SBR time step configuration of [500, 400, 200, 75, 75, 50] steps between sampling points manually chosen at the elbow point as a good compromise between numerical accuracy and computation speed. As reference for SSR calculations, a synthetic "error-free" dataset was generated by SBR using uniform 30,000-step and the best prototyping INS solution.

(E) Optimized SBR time step (red cross) still showed a good compromise between accuracy and speed when retested against actual INS solution and synthetic data generated by ODE15s (with Jacobian). Numerical error was less than theoretical error estimated from measurement noise.

See also Figures S2 and S3.

B-splines can model any flux trajectory, but careful parameterization of order and knot is needed to avoid overfitting. Thus, in parallel to model reconstruction, we tested configurations of B-splines up to orders of three, in combination with up to three internal knots (Figure 3C, see Transparent Methods). Using AIC to balance overfitting and underfitting, we found that the final adipocyte model was best modeled using quadratic fluxes (order = 3) and one internal knot. This meant four CP values were used to model each $v(t)$. The flux model had a total of 329 estimated parameters: 66 fluxes × 4, 37 initial concentrations, and 28 stagnant pools. In comparison, INS and CTRL dataset each has a total of 750 and 671 data points,

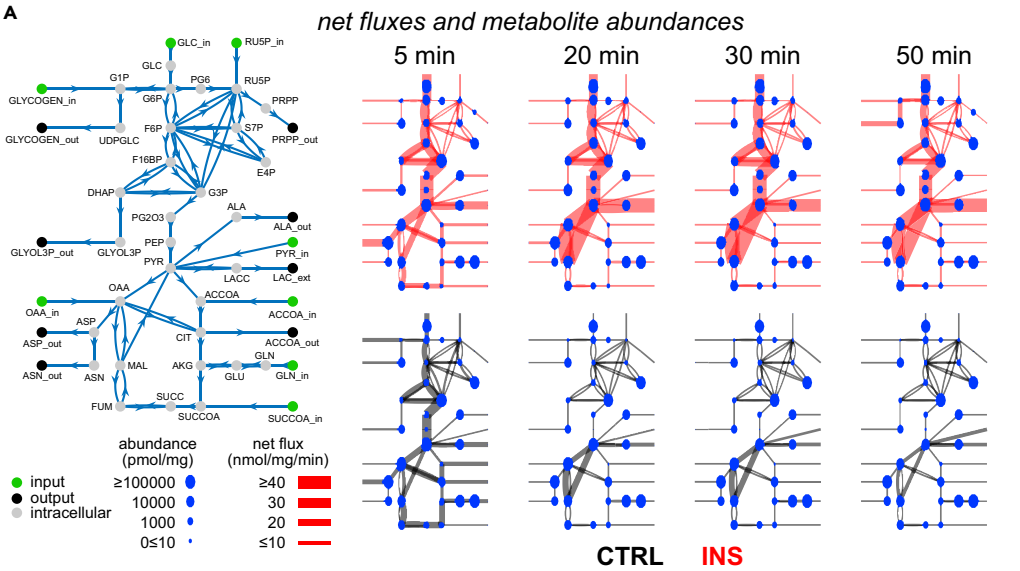
A
net fluxes and metabolite abundances
5 min
20 min
30 min
50 min
GLC_in
RU5P_in
GLC
G1P
PG6
RU5P
GLYCOGEN_in
G6P
PRPP
GLYCOGEN_out
UDPGLC
F6P
S7P
PRPP_out
F16BP
E4P
DHAP
G3P
ALA
PG2O3
ALA_out
GLYOL3P_out
GLYOL3P
PEP
PYR_in
PYR
LACC
LAC_ext
OAA
ACCOA
OAA_in
ACCOA_in
ASP
CIT
ASP_out
ACCOA_out
GLN
ASN_out
MAL
AKG
GLU
GLN_in
ASN
SUCC
FUM
SUCCOA
SUCCOA_in
abundance (pmol/mg)
net flux (nmol/mg/min)
input
output
intracellular
≥100000
10000
1000
0≤10
≥40
30
20
≤10
CTRL
INS

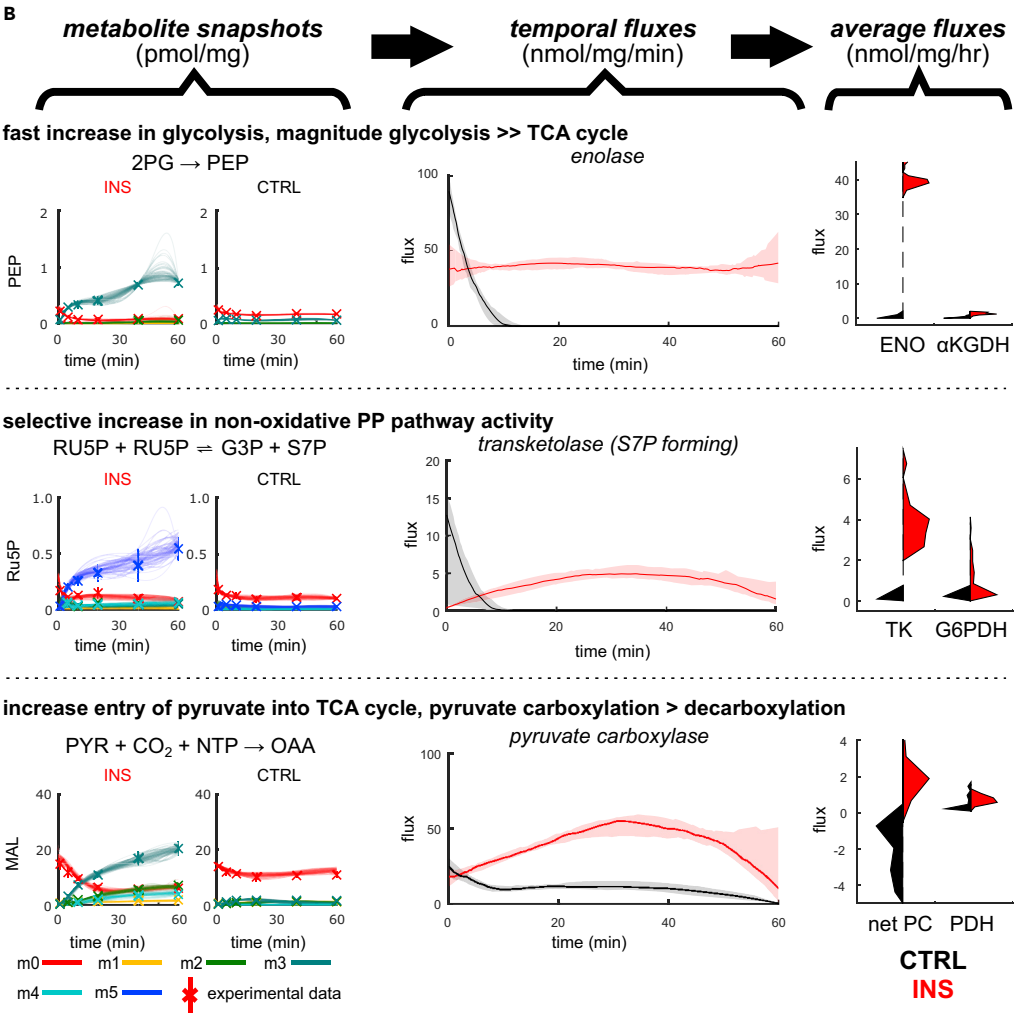
B
metabolite snapshots (pmol/mg)
temporal fluxes (nmol/mg/min)
average fluxes (nmol/mg/hr)
fast increase in glycolysis, magnitude glycolysis >> TCA cycle
2PG → PEP
INS
CTRL
PEP
time (min)
enolase
flux
ENO
αKGDH
selective increase in non-oxidative PP pathway activity
RU5P + RU5P ⇌ G3P + S7P
Ru5P
transketolase (S7P forming)
TK
G6PDH
increase entry of pyruvate into TCA cycle, pyruvate carboxylation > decarboxylation
PYR + CO2 + NTP → OAA
MAL
pyruvate carboxylase
net PC
PDH
m0
m1
m2
m3
m4
m5
experimental data

**Figure 4. Temporal Fluxes Showed Differences in Dynamics and Magnitude**

(A) Network map showing median temporal net fluxes and metabolite abundances.

(B) Isotopologue data and fitted solutions generated by Monte-Carlo (left column). Experimental data are represented as mean ±2×SEM of 3 biological replicates. Temporal fluxes generated to recapitulate the isotopologue data showed differences in flux dynamics (middle column). Line shows median flux and shaded area shows interquartile range from 50 Monte-Carlo replicates. The distributions of average fluxes show summarized differences in flux magnitude (right column). Average fluxes were calculated by integrating the area under the curve from 10 to 60 min.

See also Figure S4.

respectively; the difference is due to missing values. Underfitting was not an immediate issue as the calculated SSRs were larger than the chi-square limit.

The final prototyping task was to calibrate the SBR time steps (see Transparent Methods). The aim of this calibration task is to reduce numerical error incurred by our SBR algorithm; commercial ODE solvers implement adaptive step size to achieve this. Smaller time steps are needed to more accurately model faster rates of enrichment, thus the calibration was performed on INS rather than CTRL. Briefly, based on the best prototyping solution of INS, we substituted $data_{exp}$ with $c(t)$ and $x(t)$ to calculate $data_{sim}$. We started with a uniform 30,000 step as upper limit and tested various SBR time steps generated by a combination of grid search and random sampling, with a uniform 20-step set as the lower limit. Employing a strategy analogous to the Elbow method for clustering optima, SSRs here were used to show that [500,400,200,75,75,50] steps between sampling time points achieved a good balance between speed and accuracy (Figure 3D). Indeed, this configuration reflected that metabolite enrichments in the INS dataset were rapidly increasing within the first four time points (1–20 min). When final flux results were generated, we verified that the error incurred by this optimized set of SBR time steps was small relative to the error associated to measurement noise (Figures 2H and 3E). Compared with the uniform 20-step used for prototyping, this time step configuration was 10-fold slower; a single optimization generally took 30 h to complete (CPU 3.4 GHz).

To generate flux results in *parameter estimation* (Figure 3A), a multi-start procedure—repeating the optimization using random initial values—was implemented to address the local optimum problem of non-linear optimization (see Transparent Methods). In parallel, the multi-start procedure also sampled for different knot positions, because this parameter was set before the optimization. Thus, knot optimization incorporated both metabolite abundances and enrichments, unlike PWA. SSRs were sensitive to knot position, with CTRL knots placed early and INS knots more spread out for the lowest 20% SSRs (Figure S3C).

Despite our best efforts, we could not bring the minimum SSR for both INS and CTRL below the chi-square limits. Visually, the estimated fluxes have reproduced the respective dataset (Data S3), but the normal probability plots of the residual errors showed a slight departure from normality (Figure S3E). However, the data points with high residuals did not belong to specific pathway or metabolites (see Transparent Methods). We may have underestimated measurement uncertainties because increasing the minimum error threshold from 1% to 5% can bring SSRs down to within the chi-square limits without significantly changing the optimized solution, as the optimum solutions with 5% minimum error were still within proximity of the original Monte-Carlo solutions (Figure S3I). The application of a blanket 1% minimum error in our modeling strategy mainly reflects the expected instrument accuracy of determining relative enrichment of isotopologues (<1.5%) (Buescher et al., 2015), but this does not capture biological variance. Without any apparent systematic bias as leads to troubleshoot, we proceeded without making any further modification. Overall, this issue raised the caveat that although estimated fluxes were generally correct, they still contained systematic biases. Nonetheless, we have validated that our optimization approach was able to converge at the global optimum when challenged with a synthetic INS and CTRL dataset (Figure S3D).

Last, Monte-Carlo resampling was used to evaluate the spread of the estimated parameters; this included knot positions (Figures S3F and S3H). We generated 50 corrupted sets of metabolite data per condition, CTRL and INS, using one standard deviation of Gaussian noise, and multi-start optimization was again performed on each set. By resampling, we verified that 50 iterations were sufficient because the medians and standard deviations of the estimated parameters stabilized by the first 30 iterations of sampling (Figure S3G). By 50 samples, the standard deviations of 245 of 329 parameters have stabilized within 1% ($\Delta SD_{one\ more\ sample}/SD$). Subsequent interrogations of flux results and their distributions were based on these 2×50 solutions.

### Insulin Stimulates a Heterogeneous Metabolic Response beyond Glucose Uptake

We previously established that insulin treatment rapidly increased glucose influx and directed glucose flow in a pathway-specific manner in cultured adipocytes (Krycer et al., 2017). This was corroborated here by an elevation in metabolic fluxes across central carbon metabolism by insulin, with this effect sustained over the time course (Figure 4A). On the other hand, CTRL-treated cells exhibited initially high fluxes that decayed rapidly without insulin (Figures 4A and 4B), likely a result of media exchange (discussed in the next section).

Examining insulin-responsive changes in flux rates (INS-CTRL), we found that glycolytic flux only took 10 min to reach a new, higher steady state at about 40 nmol/mg/h (Figure 4B, Data S2). The acceleration rate of glycolysis was consistent with published extracellular acidification rates of insulin-stimulated 3T3-L1 cells (Schreiber et al., 2017). If glucose influx was the sole determinant of central carbon fluxes, we would expect that a majority of glucose-dependent ($^{13}$C-labeled) pathway fluxes rise concomitantly with glycolysis in response to insulin. However, branching pathways reached differing magnitudes (Figures 4B and S4A). For instance, pyruvate dehydrogenase (PDH) flux only increased from 0.21 to 0.72 nmol/mg/h (Figure S4A). These pathways peripheral to glycolysis also showed a more gradual ramping in response to insulin. The flux of pyruvate carboxylase (PC), transketolase (TK), and malic enzyme (ME) took about 30–40 min to reach maximum velocity (Figures 4B and S4A). Overall, these flux differences suggest that glucose metabolism is driven by more than just glucose influx.

Furthermore, these flux differences were not always evident from the metabolite data itself. For instance, metabolite abundances in both oxidative and non-oxidative arms of pentose phosphate pathway rose concurrently in response to insulin (Krycer et al., 2017), but it was TK flux that substantially increased from near zero to 4 nmol/mg/h, with G6P dehydrogenase (G6PDH) flux remaining constant at 0.2 nmol/mg/h (Figures 4B and S4A). Parenthetically, in contrast, ME flux increased 3.7-fold to 41 nmol/mg/h by insulin (Figure S4A), reinforcing previous findings that ME is the primary site of NADPH generation in adipocytes (Liu et al., 2016). Overall, this demonstrates the value of calculating fluxes to quantify pathway activity.

To explore these flux changes on a broader scale, we mapped insulin-dependent changes onto the metabolic network to understand how adipocytes handle imported glucose. This revealed that adjacent steps within pathways responded similarly to insulin but differed markedly from other pathways or even other segments within the same pathway. We reasoned that flux-controlling steps regulated this modularity. Thus, we identified modules by unsupervised K-means clustering, generating eight optimum clusters (Figures 5A, S5A, and S5B, see Transparent Methods). When overlayed onto the pathway map, this analysis revealed that segments of the glycolytic pathway responded differently to insulin (Figure 5B). For instance, the flux rates in lower glycolysis (#7) increased more rapidly than upper glycolysis (#5), the latter showing a potential overshoot. At the border between upper and lower glycolysis, the reversible aldolase and triose phosphate isomerase steps (#4) were very active. The punctuation of flux dynamics at GAPDH reinforced this enzyme as a flux-controlling step of glycolysis (Shestov et al., 2014). Thus, the enzymes downstream of glucose transport were not simply driven by glucose influx. The modular system suggested a feedforward mechanism, whereby lower glycolysis pre-emptively increased in flux before glucose transport and upper glycolysis.

Similarly, the TCA cycle was segmented, with pyruvate situated at the interface (Faubert et al., 2017). The series of enzymes converting 2-oxoglutarate to fumarate were clustered together (#2), demonstrating that the TCA cycle still operated in the canonical oxidative fashion (Figure 5B). Superimposed were the large PC and ME fluxes that were increasing together (#5), albeit more gradually, in greater magnitude than the oxidative half of the TCA cycle. The extracellular lactate m+2 fraction was unusually large (Figure S4B) and directly constrained the model to produce high cyclic pyruvate carboxylation-decarboxylation flux, a process that is coupled to pyruvate carbon being scrambled/inverted at symmetrical fumarate to produce the m+2 lactate signal (10% for CTRL, 19% for INS). This futile cyclic flux around PC and ME was insulin responsive and a potential avenue for cell to generate NADPH for lipogenesis from surplus NADH by consuming ATP.

Overall, the formation of clusters based on flux dynamics and magnitude demonstrated that adipocytes' central carbon metabolism is more complex than just a glucose overflow driven by uptake. This suggests that metabolic pathways are organized into modules to better coordinate diversion and utilization of glucose.

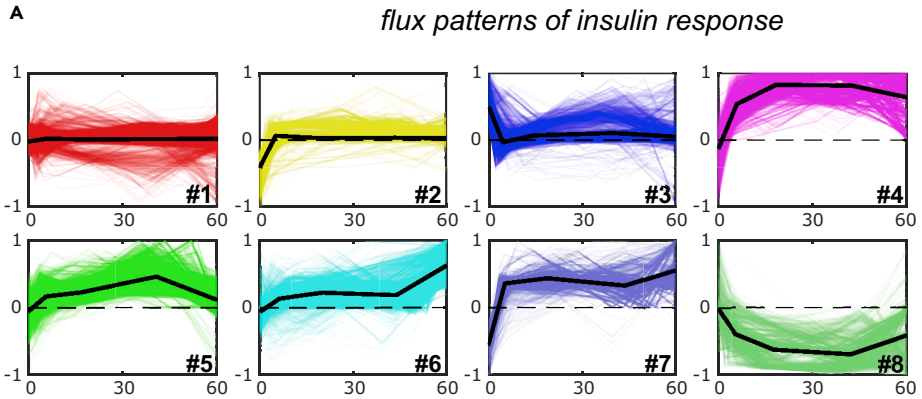


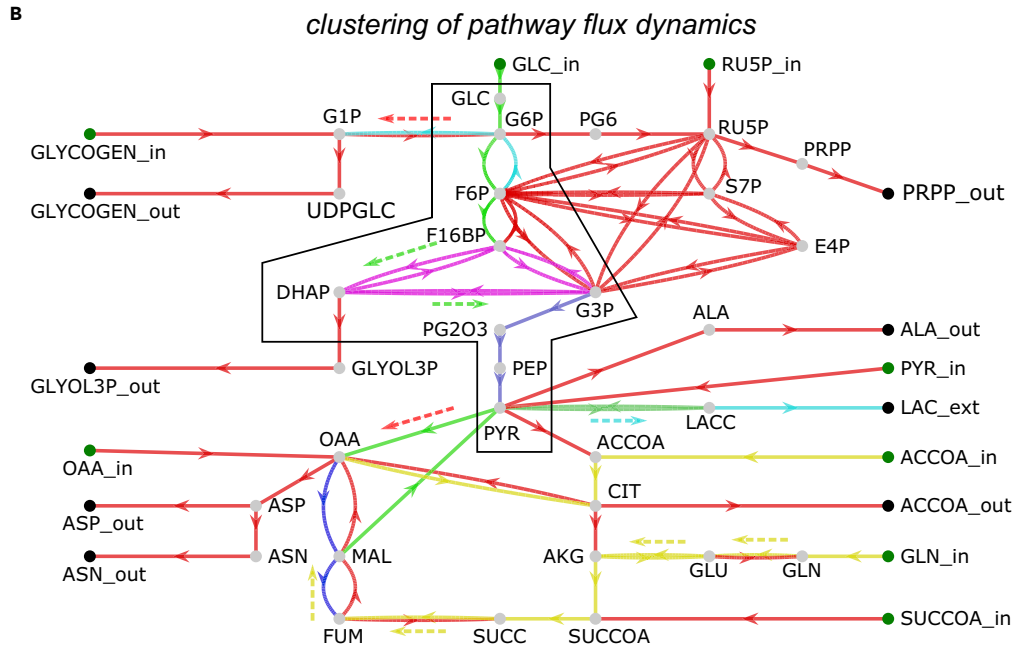


**Figure 5. Adipocyte Fluxes Responded Rapidly to Insulin in a Modular Fashion**

(A) Eight clusters of insulin responses grouped based on the control points of temporal flux differences (INS minus CTRL). The control points summarize the trajectory of each flux difference into five points in time, with the vertical axis normalized to [-1,1] using the maximum flux and the horizontal axis representing time in minutes. Black lines represent centroid location.

(B) Network reactions were colored using cluster information based on majority. Dashed arrows represent net flux. Metabolites and enzymes in the glycolysis pathway outlined.

See also Figure S5.

## The Effect of Media Exchange Depends on Insulin Pre-conditioning

We expected the CTRL cells to remain in metabolic steady state, but we observed non-steady fluxes in these cells (Figure 4B). "Constant flux" B-splines (order = 1, knots = 0) gave high SSRs (≥5,000) and AIC

scores (Figure 3C). Indeed, "hockey stick" fluxes, characterized by a high but rapidly declining flux in the first 10 min, were required to achieve fast and early enrichment of CTRL metabolites (Data S3).

We speculated that this was due to media exchange between the pre-incubation and labeling/treatment periods (Figure 6A) (Krycer et al., 2017), involving PBS and DMEM washes to maximize glucose labeling at ~100%. Based on CTRL fluxes, the effects of these perturbations dissipated within 10 min (Figures 4B and S4A). We explored this further, comparing media exchange to the effects of insulin stimulation. The abundances of central carbon metabolites under CTRL and INS conditions were analyzed using principal-component analysis (PCA). Principal component 1 (PC1) appeared to have captured the insulin-dependent evolution of metabolite levels over time (Figure 6B). Unstimulated cells CTRL-10 and CTRL-60 formed a tight cluster relative to the plotted trajectory of INS-1 to INS-60 and were proximal to INS-1 and INS-5. This indicated that metabolite abundances in the CTRL dataset appeared to have normalized quickly after media exchange, much like the transient initial fluxes (Figure 4B). Thus the effects of media exchange were neither significant nor prolonged.

We tested whether media exchange perturbed insulin-conditioned adipocytes more than untreated (naive) cells. Here, adipocytes were first exposed to insulin for 50 min, and then the culture media was exchanged from $^{12}$C- to $^{13}$C-glucose-containing media 10 min before harvesting (INS-10′). Effectively, except for INS-10′, all media exchanges performed were on adipocytes in the naive state (Figure 6A). The distance between INS-60′ and INS-10′ indicated that the metabolic perturbations by media exchange were significant in adipocytes with an established insulin response (Figure 6B). The direction of shift along PC2 indicated that the perturbations were very different from insulin responses observed in naive adipocytes. These differences, and the proximity of INS-1, INS-5, and INS-10 to the cluster of CTRL data points, provide evidence that the flux differences between INS and CTRL data were principally insulin responses. This validates our pathway clustering approach (Figure 5A).

Examining the glycolytic metabolites, media exchange prominently increased fructose 1,6-bisphosphate, glyceraldehyde 3-phosphate (G3P), and dihydroxyacetone phosphate levels in insulin-conditioned, but not naive, adipocytes (Figure 6C). These metabolites are upstream of GAPDH and are enriched by exogenous glucose (Figure 6E). This suggested that media exchange caused a constriction of glucose catabolism at GAPDH, and the effects were more apparent when glycolytic flux was high. The reciprocal depletion and accumulation of nucleotide tri- and monophosphates, respectively, (Figure 6C) decreased the energy charge (Figure 6D), supporting an imbalance between upper and lower glycolysis. This resembles the "phosphate stress" phenomenon seen in yeast (van Heerden et al., 2014). In contrast, naive adipocytes did not show these responses to media exchange (Figures 6C and 6D). Overall, this further demonstrated that GAPDH is a flux-controlling step of glycolysis.

### Insulin Switched Adipocytes' Substrates to Glucose

Last, we complemented our flux analysis with carbon book-keeping, enabling us to determine the primary fates of glucose. While insulin increased the incorporation of glucose carbon into most metabolites (Figure 7A), the majority ended up as lactate at 58%, followed by glycogen at 17%. Despite being fat cells, the conversion of glucose into lipogenic acetyl-CoA, determined by radiolabeling methods, was trivial at less than 2%, with or without insulin. Lipogenesis did not appear to be a significant sink for NADPH to balance out the large ME flux, although our estimates appeared consistent with previous studies (Crown et al., 2015; Green et al., 2016). Furthermore, glucose oxidation rates (incorporation of $^{14}$C-labeled glucose into $CO_2$) were significantly smaller than the lactate production rate (Figure 7B).

In contrast, in the unstimulated state, 52% glucose carbon consumed lingered as intracellular glucose (22%), G3P (12%), and other metabolites (18%), with a further 33% converted into lactate (Figure 7A). We then used the flux models to extrapolate for the fates of non-glucose substrates (see Transparent Methods). The results showed that TCA metabolites and lactate came from a variety of sources in unstimulated adipocytes, but these sources were displaced by glucose upon insulin stimulation (Figure 7C). Insulin constricted the uptake of non-glucose substrates, namely, glutamine and pyruvate (Figure 7D). For instance, the shift from glutaminolysis to pyruvate anaplerosis by insulin was indicated by the increase of net pyruvate carboxylation flux (PC minus ME flux) from −1.8 to 1.5 nmol/mg/h (Figure 4B). The large interconversion between pyruvate, malate, and oxaloacetate caused a significant assimilation of unlabeled

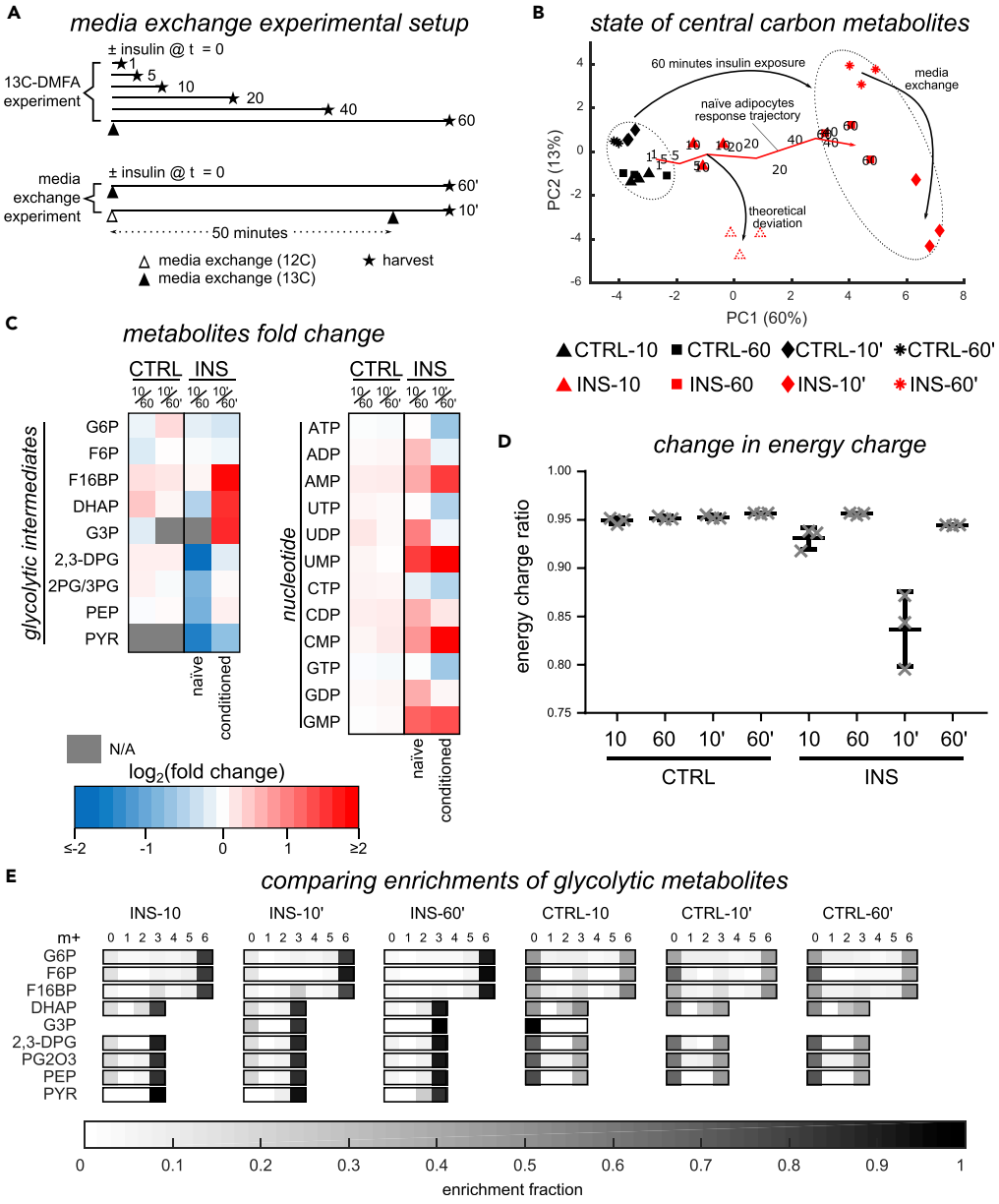


**Figure 6. The Effects of Media Exchange Exacerbated by Insulin Preconditioning**

(A) Media exchange experimental design, showing the timings of media exchange and harvest, contrasted against the main 13C-DMFA experiment. Conditioned adipocytes denoted by the prime symbol (′).

(B) PCA plot of total abundances of central carbon metabolites (in triplicates). The ellipses demarcate the two groups of adipocytes, naive and conditioned. INS-10 did not deviate from the insulin response trajectory captured by PC1, whereas metabolite abundances of INS-10′ and INS-60′ were markedly different.

(C) Heatmap compares fold changes of metabolite levels between naive and conditioned adipocytes, showing build-up of metabolites above GAPDH and mononucleotides in conditioned adipocytes. 2,3-DPG: 2,3-bisphosphoglycerate.

(D) Energy charge ratios summarize changes of nucleotide levels, showing a significant drop in energy charge when media exchange was performed on conditioned adipocyte (INS-10′). Data are represented as mean ± SD of 3 biological replicates.

(E) Relative enrichment of glycolytic metabolites at 10 min. INS-10′ enrichments suggest that flux constriction at GAPDH was partial and glucose was still catabolized to pyruvate.

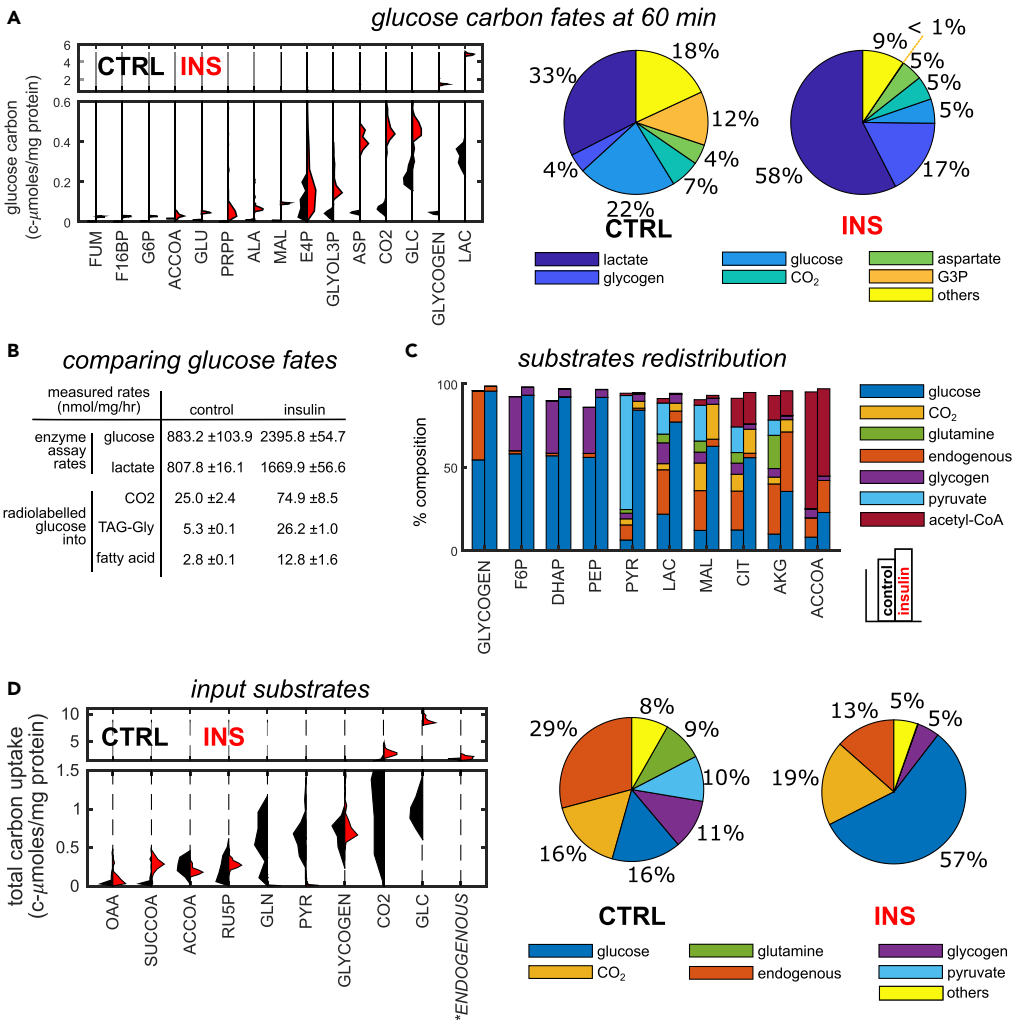


**Figure 7. Insulin Altered the Profile of Substrates' Fates**

(A) The fates of glucose carbon, showing the increased conversion of glucose into lactate and glycogen. Pie charts report median percentages of glucose carbon contained in the various end products.

(B) The partitioning of radiolabeled glucose into end products $CO_2$, glycerol (TAG-Gly), and fatty acid. These pools constituted a small fraction of the glucose consumed compared with lactate efflux determined by enzymatic assay. Data are represented as mean ± SEM of 3 biological replicates.

(C) The simulated redistribution profile of adipocytes' major substrates at 60 min. The partial penetration of glucose into TCA cycle metabolites compared with glycolytic metabolites shows that the increase in glucose oxidation by the TCA cycle was relatively small compared with aerobic glycolysis.

(D) Unstimulated adipocytes showed a mixed substrate profile, with insulin subsequently shifting carbon sources away from glutamine and pyruvate to glucose. The endogenous pool represents all the metabolites present before the addition of glucose label and is a significant carbon source. Pie charts report medians of carbon uptakes.

$CO_2$. Overall, the analysis of substrate fates suggested that insulin treatment reprogrammed adipocytes to preferentially catabolize glucose.

## DISCUSSION

In this study, we have developed a 13C-DMFA workflow to estimate non-steady-state fluxes from temporal tracer metabolite data. The incorporation of B-splines and SBR was instrumental to overcome the computational challenges faced when modeling fluxes in central carbon metabolism. The built-in algorithm can model a variety of flux trajectories (e.g., ramp, decline, sigmoidal, and even no change). The provided MATLAB package simplifies the user's task to input manipulation and prototyping (Figures

1E and 3A). Here, we used 13C-DMFA to mechanistically interpret adipocyte metabolite data, showcasing that the adipocyte dynamically coordinates numerous metabolic pathways to efficiently process glucose in response to insulin.

Our analysis revealed a heterogeneous response to insulin, with segments of metabolic pathways being differentially regulated by insulin (Figure 5B). The different flux dynamics between upper and lower glycolysis implicated the role of GAPDH in regulating glycolytic fluxes in an insulin-dependent manner. This corroborates our previous observations that insulin exerts a coordinated response at multiple sites beyond GLUT4 to regulate adipocyte metabolism (Humphrey et al., 2013; Krycer et al., 2017; Ma et al., 2015). It extends the concept of anabolic priming, complementing the demand-driven diversion of glucose into appropriate sinks through fast protein phosphorylation events independently of glucose supply. Altogether, this work demonstrates the value of acute tracer experiments in generating testable hypotheses pertinent to metabolic regulation.

In particular, 13C-DMFA enabled us to compare the speed and magnitude of pathway fluxes and facilitated detailed carbon book-keeping (Figures 4A and 7A). This revealed that glycolysis operated faster than the TCA cycle and that a major fate of glucose was lactate, together suggesting that aerobic glycolysis is a major metabolic trait of adipocyte metabolism. Indeed, a preference for lactate production has been well documented in primary adipocytes (DiGirolamo et al., 1992). Furthermore, aerobic glycolysis is a cancer hallmark (Pavlova and Thompson, 2016; Vander Heiden and DeBerardinis, 2017), and may also be utilized here in terminally differentiated adipocytes to facilitate insulin-stimulated anabolism.

Another rationale is that lactate production enables the rate of glycolysis to be rapidly elevated independently of other pathways (Hui et al., 2017). In our data, glycolysis achieved substantially higher fluxes than the oxidative TCA cycle and peripheral pathways (Figure 4A), with an acceleration matching the dynamics of GLUT4 trafficking (Burchfield et al., 2013) and glucose uptake (Krycer et al., 2017) in response to insulin. Thus, aerobic glycolysis serves to cater for the large glucose influx upon insulin stimulation.

Exploring this further, we challenged insulin-stimulated adipocytes with media exchange, finding a significant drop in energy charge. This demonstrates the importance of prioritizing ATP harvesting before ramping up glycolysis because glycolysis is an autocatalytic cycle that has inherent potential to be unstable (Barenholz et al., 2017). GAPDH regulation is a safeguard against glycolysis stalling (van Heerden et al., 2014), but GAPDH itself was prone to disruption when glycolytic flux was high (Figures 6C and 6D). Parenthetically, although fluxes were perturbed by media exchange, the effect has no bearing on previous observations of metabolic priming based on metabolite data (Krycer et al., 2017), because naive adipocytes 10 min after media exchange stayed on course (Figure 6B).

Collectively, this suggests that adipocyte metabolism is rewired in response to insulin to cater for the rapid influx of glucose, diverting glucose into relevant pathways, preventing ATP stress, and perhaps utilization of lactate dehydrogenase to maintain cytosolic redox status. Future investigations should explore how these metabolic responses by the adipocyte change with varying glucose availability, including insulin resistance where glucose uptake is impaired.

Overall, 13C-DMFA caters for tracer experiments examining non-steady-state metabolism, its utility demonstrated through the temporal resolution of insulin responses at the intracellular flux level. We envisage that 13C-DMFA can be integrated or cross-validated with other datasets, such as gene expression and protein modification data, to dissect how enzyme levels, allostery, and post-translational modifications interact to acutely regulate metabolism.

## Limitations of the Study

Our approach provides a substantial improvement on existing approaches to quantify dynamic flux rates. Nonetheless, there are future avenues for improvement. For instance, we did not achieve statistically acceptable fit as the minimum SSRs were greater than the chi-square critical value. This indicated the presence of systematic biases in the model and/or data that were not apparent, or we have underestimated the uncertainties of the experimental data. A potential source of bias was the adoption of a single-compartment model to avoid overfitting, which can impact interpretation of labeling dynamics when metabolite production has significant compartment

dependency (Buescher et al., 2015). However, the methodology itself is sound because it can find true solutions (Figure S3D), and the use of AIC to optimize B-spline order and number of knots provided countermeasure against overfitting (Figure 3C). Furthermore, our model can be adapted to improvements in metabolite detection, such as the incorporation of compartmentalization in metabolomics data.

## METHODS

All methods can be found in the accompanying Transparent Methods supplemental file.

## DATA AND CODE AVAILABILITY

The metabolic model and intracellular metabolite datasets are provided in Data S1. MATLAB scripts and adipocyte data are made available as a GitHub repository (https://github.com/lakeeeq/OpenFLUX). The scripts provided are for the adipocyte dataset as Data S4, but can be customized for other datasets. It is based on OpenFLUX's framework but can run independently (Quek et al., 2009).

## SUPPLEMENTAL INFORMATION

Supplemental Information can be found online at https://doi.org/10.1016/j.isci.2020.100855.

## ACKNOWLEDGMENTS

This work was supported by National Health and Medical Research Council (NHMRC) program grants (GNT1061122 and GNT1086850 for D.E.J.). L.E.Q. was funded by the Judith and David Coffey Fund and Cancer Institute NSW (CDF181241). J.R.K. was funded by an NHMRC Early Career Fellowship (APP1072440), Australian Diabetes Society Skip Martin Early Career Fellowship, and Diabetes Australia Research Project grant. D.E.J. is an NHMRC Senior Principal Research Fellow (APP1019680). S.K. was supported by the Creation of Fundamental Technologies for Understanding and Control of Biosystem Dynamics, CREST (JPMJCR12W3) from the Japan Science and Technology Agency (JST) and by the Japan Society for the Promotion of Science (JSPS) KAKENHI Grant Number 17H06300. T.S. was funded by the AMED-CREST from AMED, and from Yamagata prefectural government and the City of Tsuruoka. This research was supported by the Sydney Informatics Hub, funded by the University of Sydney. This research was facilitated by access to Sydney Mass Spectrometry, a core research facility at the University of Sydney. The contents of the published material are solely the responsibility of the authors and do not reflect the views of the NHMRC. K.Y. receives funding from the JSPS (KAKENHI grant numbers JP15H05582 and JP18H05431) and PRESTO (JPMJPR1538) from the JST.

## AUTHOR CONTRIBUTIONS

Conceptualization, L.E.Q. and J.R.K.; Methodology, L.E.Q.; Software, L.E.Q.; Formal analysis, L.E.Q. and J.R.K.; Investigation, L.E.Q., J.R.K., D.J.F., S.D.E., A.H., S.I., F.S., and K.S.; Resources, T.S., S.K., and D.E.J.; Writing – Original Draft, L.E.Q., J.R.K., S.K., and D.E.J.; Writing – Review & Editing, all authors; Visualization, L.E.Q. and J.R.K.; Supervision, S.K. and D.E.J.; Fund Acquisition, J.R.K., S.K., and D.E.J.

## DECLARATION OF INTERESTS

The authors declare no competing interests.

Received: July 17, 2019
Revised: November 26, 2019
Accepted: January 15, 2020
Published: February 21, 2020

## REFERENCES

Abate, A., Hillen, R.C., and Aljoscha Wahl, S. (2012). Piecewise affine approximations of fluxes and enzyme kinetics from in vivo 13C labeling experiments. Int. J. Robust. Nonlin. *22*, 1120–1139.

Alves, T.C., Pongratz, R.L., Zhao, X.J., Yarborough, O., Sereda, S., Shirihai, O., Cline, G.W., Mason, G., and Kibbey, R.G. (2015). Integrated, step-wise, mass-isotopomeric flux analysis of the TCA cycle. Cell Metab. *22*, 936–947.

Antoniewicz, M.R. (2018). A guide to (13)C metabolic flux analysis for the cancer biologist. Exp. Mol. Med. *50*, 19.

Antoniewicz, M.R., Kelleher, J.K., and Stephanopoulos, G. (2007). Elementary metabolite units (EMU): a novel framework for modeling isotopic distributions. Metab. Eng. *9*, 68–86.

Barenholz, U., Davidi, D., Reznik, E., Bar-On, Y., Antonovsky, N., Noor, E., and Milo, R.

(2017). Design principles of autocatalytic cycles constrain enzyme kinetics and force low substrate saturation at flux branch points. Elife *6*, e20667.

Buescher, J.M., Antoniewicz, M.R., Boros, L.G., Burgess, S.C., Brunengraber, H., Clish, C.B., DeBerardinis, R.J., Feron, O., Frezza, C., Ghesquiere, B., et al. (2015). A roadmap for interpreting (13)C metabolite labeling patterns from cells. Curr. Opin. Biotechnol. *34*, 189–201.

Burchfield, J.G., Lu, J.L., Fazakerley, D.J., Tan, S.X., Ng, Y., Mele, K., Buckley, M.J., Han, W.P., Hughes, W.E., and James, D.E. (2013). Novel systems for dynamically assessing insulin action in live cells reveals heterogeneity in the insulin response. Traffic *14*, 259–273.

Cordes, T., and Metallo, C.M. (2016). Tracing insights into human metabolism using chemical engineering approaches. Curr. Opin. Chem. Eng. *14*, 72–81.

Crown, S.B., Marze, N., and Antoniewicz, M.R. (2015). Catabolism of branched chain amino acids contributes significantly to synthesis of odd-chain and even-chain fatty acids in 3T3-L1 adipocytes. PLoS One *10*, e0145850.

Dai, Z., and Locasale, J.W. (2017). Understanding metabolism with flux analysis: from theory to application. Metab. Eng. *43*, 94–102.

DiGirolamo, M., Newby, F.D., and Lovejoy, J. (1992). Lactate production in adipose tissue: a regulated function with extra-adipose implications. FASEB J. *6*, 2405–2412.

Faubert, B., Li, K.Y., Cai, L., Hensley, C.T., Kim, J., Zacharias, L.G., Yang, C.D., Do, Q.N., Doucette, S., Burguete, D., et al. (2017). Lactate metabolism in human lung tumors. Cell *171*, 358–371.

Green, C.R., Wallace, M., Divakaruni, A.S., Phillips, S.A., Murphy, A.N., Ciaraldi, T.P., and Metallo, C.M. (2016). Branched-chain amino acid catabolism fuels adipocyte differentiation and lipogenesis. Nat. Chem. Biol. *12*, 15–21.

Green, H., and Kehinde, O. (1975). An established preadipose cell line and its differentiation in culture. II. Factors affecting the adipose conversion. Cell *5*, 19–27.

Horl, M., Schnidder, J., Sauer, U., and Zamboni, N. (2013). Non-stationary C-13-Metabolic flux ratio analysis. Biotechnol. Bioeng. *110*, 3164–3176.

Hui, S., Ghergurovich, J.M., Morscher, R.J., Jang, C., Teng, X., Lu, W., Esparza, L.A., Reya, T., Le, Z., Yanxiang Guo, J., et al. (2017). Glucose feeds the TCA cycle via circulating lactate. Nature *551*, 115–118.

Humphrey, S.J., Yang, G., Yang, P.Y., Fazakerley, D.J., Stockli, J., Yang, J.Y., and James, D.E. (2013). Dynamic adipocyte phosphoproteome reveals that Akt directly regulates mTORC2. Cell Metab. *17*, 1009–1020.

Kogadeeva, M., and Zamboni, N. (2016). SUMOFLUX: a generalized method for targeted 13C metabolic flux ratio analysis. PLoS Comput. Biol. *12*, e1005109.

Koh, H.J., Lee, S.M., Son, B.G., Lee, S.H., Ryoo, Z.Y., Chang, K.T., Park, J.W., Park, D.C., Song, B.J., Veech, R.L., et al. (2004). Cytosolic NADP+-dependent isocitrate dehydrogenase plays a key role in lipid metabolism. J. Biol. Chem. *279*, 39968–39974.

Kotte, O., Zaugg, J.B., and Heinemann, M. (2010). Bacterial adaptation through distributed sensing of metabolic fluxes. Mol. Syst. Biol. *6*, 355.

Krycer, J.R., Yugi, K., Hirayama, A., Fazakerley, D.J., Quek, L.E., Scalzo, R., Ohno, S., Hodson, M.P., Ikeda, S., Shoji, F., et al. (2017). Dynamic metabolomics reveals that insulin primes the adipocyte for glucose metabolism. Cell Rep. *21*, 3536–3547.

Lee, H.J., Jedrychowski, M.P., Vinayagam, A., Wu, N., Shyh-Chang, N., Hu, Y., Min-Wen, C., Moore, J.K., Asara, J.M., Lyssiotis, C.A., et al. (2017). Proteomic and metabolomic characterization of a mammalian cellular transition from Quiescence to proliferation. Cell Rep. *20*, 721–736.

Link, H., Fuhrer, T., Gerosa, L., Zamboni, N., and Sauer, U. (2015). Real-time metabolome profiling of the metabolic switch between starvation and growth. Nat. Methods *12*, 1091–1097.

Liu, L., Shah, S., Fan, J., Park, J.O., Wellen, K.E., and Rabinowitz, J.D. (2016). Malic enzyme tracers reveal hypoxia-induced switch in adipocyte NADPH pathway usage. Nat. Chem. Biol. *12*, 345–352.

Liu, X., and Locasale, J.W. (2017). Metabolomics: a primer. Trends Biochem. Sci. *42*, 274–284.

Ma, D.K., Stolte, C., Krycer, J.R., James, D.E., and O'Donoghue, S.I. (2015). SnapShot: insulin/IGF1 signaling. Cell *161*, 948–948.e1.

Martínez, V.S., Buchsteiner, M., Gray, P., Nielsen, L.K., and Quek, L.E. (2015). Dynamic metabolic flux analysis using B-splines to study the effects of temperature shift on CHO cell metabolism. Metab. Eng. Commun. *2*, 46–57.

O'Brien, E.J., Monk, J.M., and Palsson, B.O. (2015). Using genome-scale models to predict biological capabilities. Cell *161*, 971–987.

Pavlova, N.N., and Thompson, C.B. (2016). The emerging hallmarks of cancer metabolism. Cell Metab. *23*, 27–47.

Quek, L.E., Dietmair, S., Kromer, J.O., and Nielsen, L.K. (2010). Metabolic flux analysis in mammalian cell culture. Metab. Eng. *12*, 161–171.

Quek, L.E., Wittmann, C., Nielsen, L.K., and Kromer, J.O. (2009). OpenFLUX: efficient modelling software for 13C-based metabolic flux analysis. Microb. Cell Fact. *8*, 25.

Schreiber, I., Dorpholz, G., Ott, C.E., Kragesteen, B., Schanze, N., Lee, C.T., Kohrle, J., Mundlos, S., Ruschke, K., and Knaus, P. (2017). BMPs as new insulin sensitizers: enhanced glucose uptake in mature 3T3-L1 adipocytes via PPAR gamma and GLUT4 upregulation. Sci. Rep. *7*, 17192.

Schumacher, R., and Wahl, S.A. (2015). Effective estimation of dynamic metabolic fluxes using (13) C labeling and piecewise affine approximation: from theory to practical applicability. Metabolites *5*, 697–719.

Shestov, A.A., Liu, X.J., Ser, Z., Cluntun, A.A., Hung, Y.P., Huang, L., Kim, D., Le, A., Yellen, G., Albeck, J.G., et al. (2014). Quantitative determinants of aerobic glycolysis identify flux through the enzyme GAPDH as a limiting step. Elife *3*, e03342.

van Heerden, J.H., Wortel, M.T., Bruggeman, F.J., Heijnen, J.J., Bollen, Y.J., Planque, R., Hulshof, J., O'Toole, T.G., Wahl, S.A., and Teusink, B. (2014). Lost in transition: start-up of glycolysis yields subpopulations of nongrowing cells. Science *343*, 1245114.

Vander Heiden, M.G., and DeBerardinis, R.J. (2017). Understanding the intersections between metabolism and cancer biology. Cell *168*, 657–669.

Vercammen, D., Logist, F., and Van Impe, J. (2014). Dynamic estimation of specific fluxes in metabolic networks using non-linear dynamic optimization. BMC Syst. Biol. *8*, 132.

Wegner, A., Meiser, J., Weindl, D., and Hiller, K. (2015). How metabolites modulate metabolic flux. Curr. Opin. Biotechnol. *34*, 16–22.

Weitzel, M., Noh, K., Dalman, T., Niedenfuhr, S., Stute, B., and Wiechert, W. (2013). 13CFLUX2-high-performance software suite for C-13-metabolic flux analysis. Bioinformatics *29*, 143–145.

Wiechert, W., and de Graaf, A.A. (1997). Bidirectional reaction steps in metabolic networks: I. Modeling and simulation of carbon isotope labeling experiments. Biotechnol. Bioeng. *55*, 101–117.

Wiechert, W., Mollney, M., Petersen, S., and de Graaf, A.A. (2001). A universal framework for $^{13}$C metabolic flux analysis. Metab. Eng. *3*, 265–283.

Young, J.D. (2014). INCA: a computational platform for isotopically non-stationary metabolic flux analysis. Bioinformatics *30*, 1333–1335.

Yuan, J., Bennett, B.D., and Rabinowitz, J.D. (2008). Kinetic flux profiling for quantitation of cellular metabolic fluxes. Nat. Protoc. *3*, 1328–1340.

Yugi, K., Ohno, S., Krycer, J.R., James, D.E., and Kuroda, S. (2019). Rate-oriented trans-omics: integration of multiple omic data on the basis of reaction kinetics. Curr. Opin. Syst. Biol. *15*, 109–120.

**iScience, Volume *23***

## Supplemental Information

# Dynamic $^{13}C$ Flux Analysis Captures the Reorganization of Adipocyte Glucose Metabolism in Response to Insulin

**Lake-Ee Quek, James R. Krycer, Satoshi Ohno, Katsuyuki Yugi, Daniel J. Fazakerley, Richard Scalzo, Sarah D. Elkington, Ziwei Dai, Akiyoshi Hirayama, Satsuki Ikeda, Futaba Shoji, Kumi Suzuki, Jason W. Locasale, Tomoyoshi Soga, David E. James, and Shinya Kuroda**

## Supplemental Figures and Legends

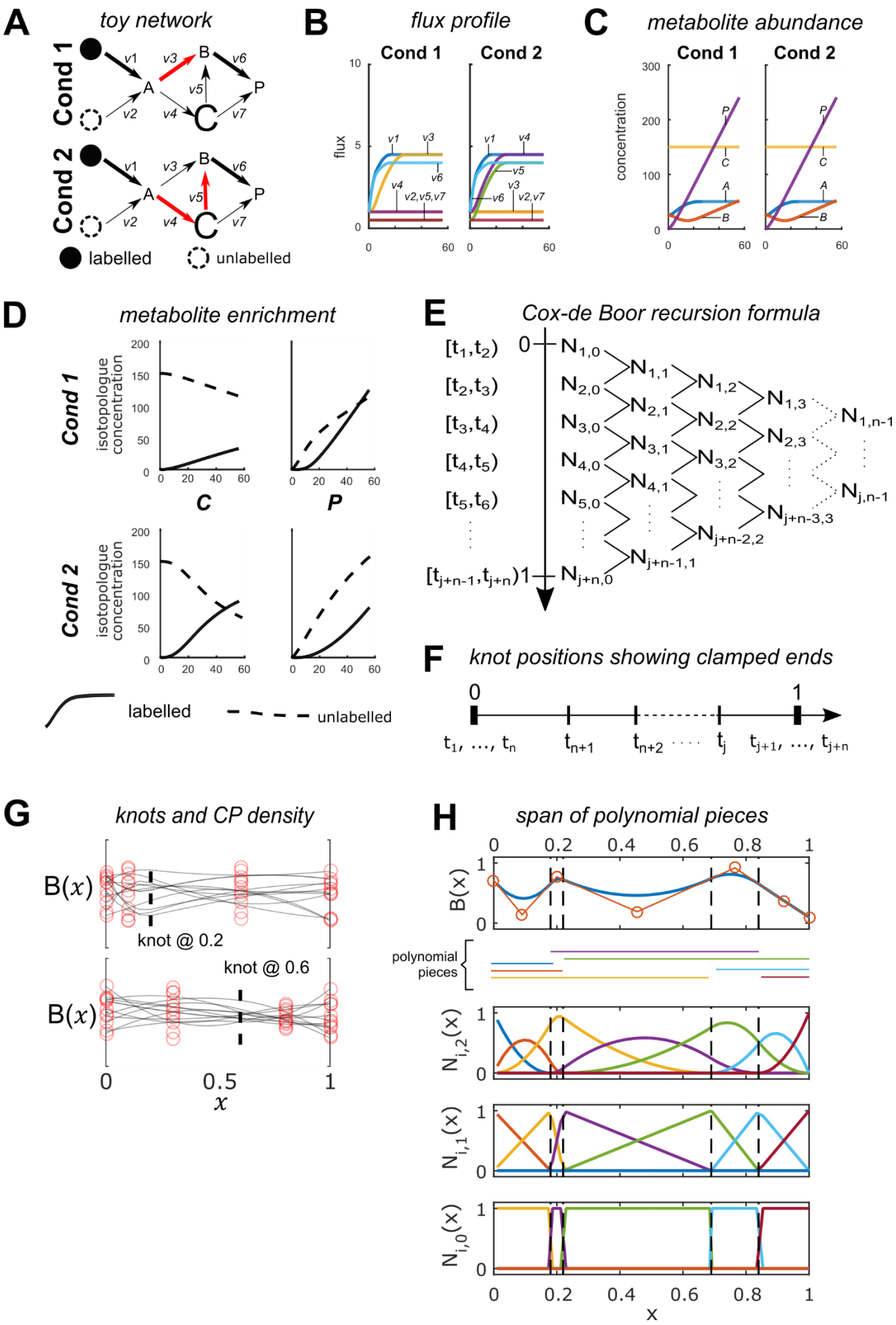
A
toy network
Cond 1
Cond 2
v1
v2
v3
v4
v5
v6
v7
A
B
C
P
labelled
unlabelled
B
flux profile
Cond 1
Cond 2
flux
C
metabolite abundance
concentration
D
metabolite enrichment
isotopologue concentration
labelled
unlabelled
E
Cox-de Boor recursion formula
F
knot positions showing clamped ends
G
knots and CP density
B(x)
knot @ 0.2
knot @ 0.6
x
H
span of polynomial pieces
polynomial pieces
x

**Figure S1**. Simulating dynamic fluxes using B-splines, Related to Figure 1.

(A) Toy problem to demonstrate the value of enrichment data. The flux from A to B, when re-routed from v3 (Condition 1) to v4 and v6 (Condition 2), goes through a large C pool.

(B) The temporal fluxes for Condition 1 and Condition 2.

(C) Temporal metabolite abundances were identical between Condition 1 and 2.

(D) Metabolite enrichment data can resolve the differences between Condition 1 and Condition 2 because isotopologue concentrations of C and P were different due to the lag introduced by the presence of a large unlabelled (endogenous) C pool.

(E) The coefficient matrix N used to produce B-spline is calculated using a tree-like approach based on the given knot position (represented as vector $t$). The order of B-spline determines the number of recursion starting from 0. The rows of the coefficient matrix are composed N's at the tree level where the recursion stops.

(F) Knot sequence plotted on a time line. Knot multiplicity (i.e., placing as many knots as the order of spline) produces clamped ends such that the resulting B-spline starts and finishes at the terminal control points.

(G) The position of knots is used to control the x-coordinate of CPs.

(H) Graphs show N's from panel E plotted in 7 different coloured pieces, with knot position marked as dashed vertical lines. Knots determine the local support of CPs; each CP's span is shown above $N_{i,2}(x)$. B(x) represents the final B-spline calculated by linear combination.

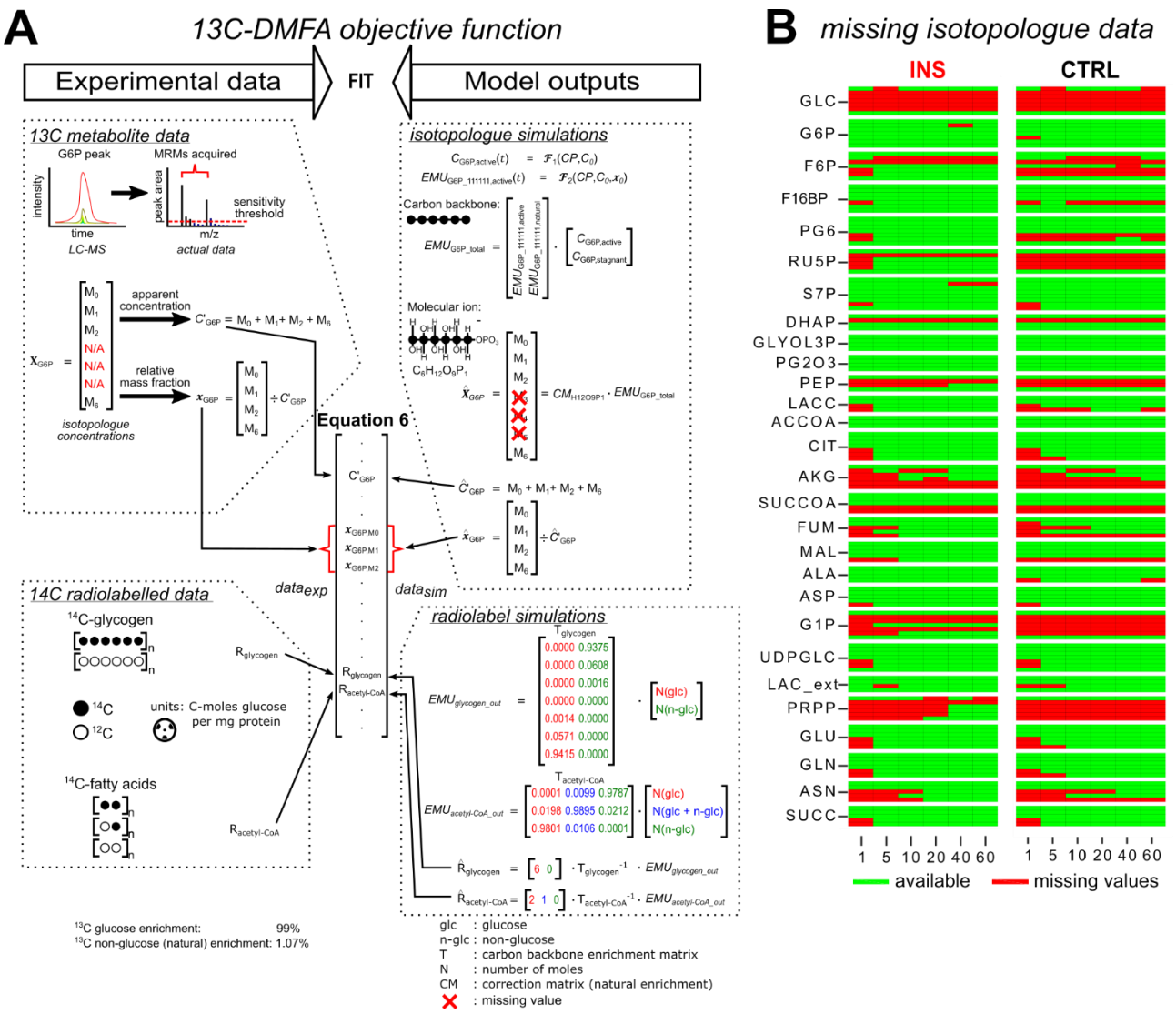


**Figure S2**. Construction of the 13C-DMFA least-square objective function, Related to Figure 3.

(A) The objective function is produced programmatically according to the available data. Due to instrument sensitivity threshold and natural isotopes, isotopologues acquired are less than what exists. Available isotopologues (*X*) were converted into apparent concentration (*C*') and relative mass fractions ($x$). The largest mass fraction is omitted. Simulated isotopologues were first calculated using EMUs and abundances, the stagnant pools, and the correction matrix (*CM*) for natural interferences, and then converted into apparent concentration and relative mass fraction using experimental data's format. $C_{i,stagnant}$ is the nuisance factor to account for the contribution of persistently unlabelled partition. $EMU_{i\_111111}$ is expressed as fractions, whereas $EMU_{i\_total}$ represents isotopologue concentrations. For radiolabelled data, EMUs can be transformed to match 14C-glucose derived substrate contributions estimates (*R*). The transformation matrix *T* specifies the one-step conversion of glucose and non-glucose carbons into the EMU of interest.

(B) INS and CTRL metabolite enrichment data sets showing the presence of missing values.

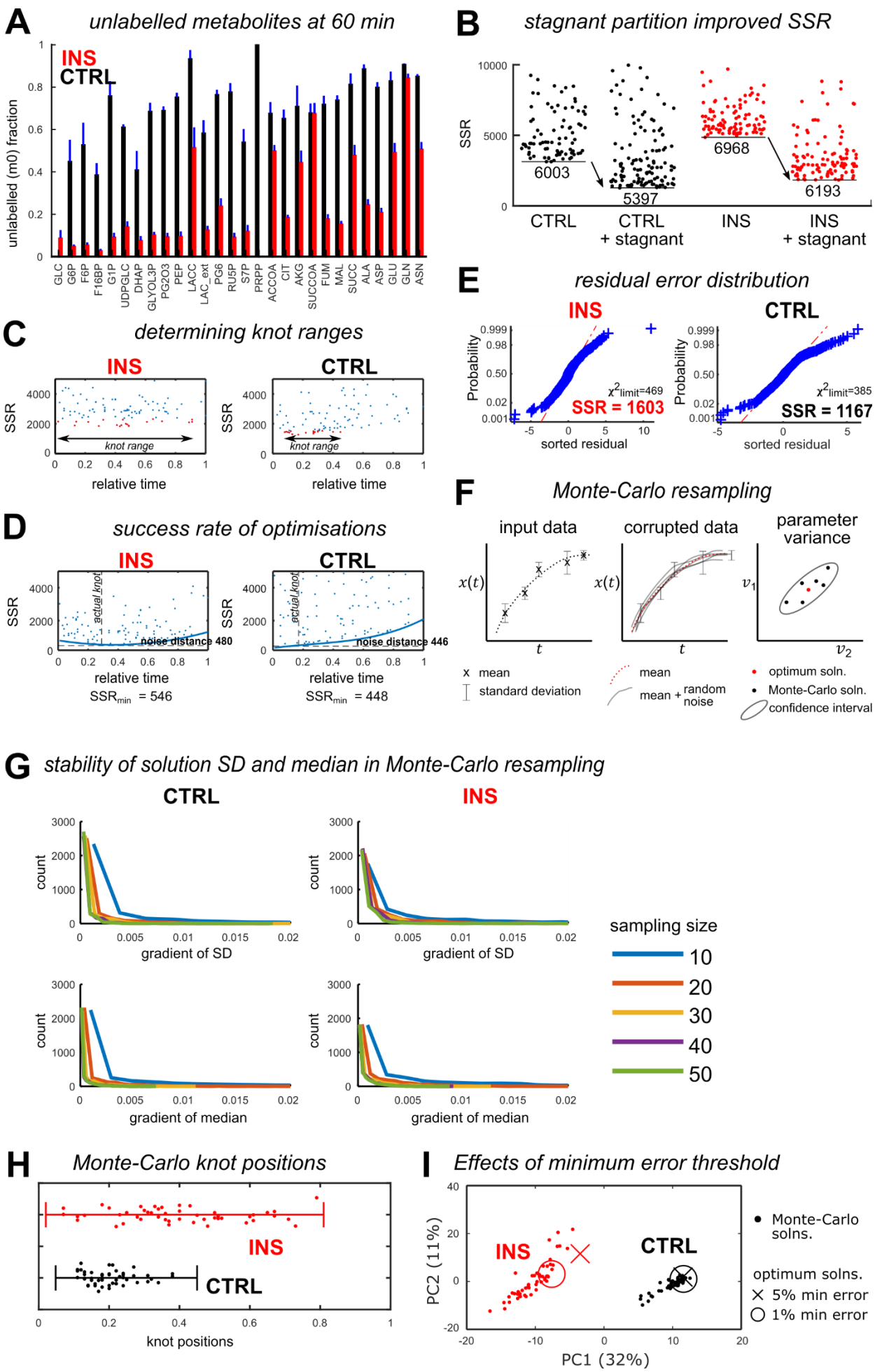
A
unlabelled metabolites at 60 min
INS
CTRL
unlabelled (m0) fraction
GLC G6P F6P F16BP G1P UDPGLC DHAP GLYOL3P PG2O3 PEP LACC LAC_ext PG6 RU5P S7P PRPP ACCOA CIT AKG SUCCOA FUM MAL SUCC ALA ASP GLU GLN ASN
B
stagnant partition improved SSR
SSR
6003
5397
6968
6193
CTRL
CTRL + stagnant
INS
INS + stagnant
C
determining knot ranges
INS
CTRL
SSR
knot range
relative time
D
success rate of optimisations
INS
CTRL
actual knot
noise distance 480
noise distance 446
relative time
SSR_min = 546
SSR_min = 448
E
residual error distribution
INS
CTRL
Probability
sorted residual
x²limit=469
SSR = 1603
x²limit=385
SSR = 1167
F
Monte-Carlo resampling
input data
corrupted data
parameter variance
x(t)
t
v1
v2
x mean
standard deviation
mean
mean + random noise
optimum soln.
Monte-Carlo soln.
confidence interval
G
stability of solution SD and median in Monte-Carlo resampling
CTRL
INS
count
gradient of SD
gradient of median
sampling size
10
20
30
40
50
H
Monte-Carlo knot positions
INS
CTRL
knot positions
I
Effects of minimum error threshold
INS
CTRL
PC2 (11%)
PC1 (32%)
Monte-Carlo solns.
optimum solns.
5% min error
1% min error

**Figure S3**. Problems addressed during prototyping, Related to Figure 3.

(A) The unlabelled fractions of metabolites at 60 minutes. Despite fast turnover rates, a significant fraction of glycolytic metabolites remained unlabelled, more so for control cultures. Data are represented as mean ± 2×SEM of 3 biological replicates.

(B) Incorporating stagnant partitions as estimated parameters in the optimisation improved fit. The best AIC values for each set are shown below the minimum line.

(C) Placement of knots during prototyping. CTRL knots were sensitive to SSRs and were placed earlier than INS.

(D) When challenged with corrupted INS and CTRL synthetic datasets, the optimisation procedure returned minimum SSRs that were consistent with noise residuals, and reproduced actual knot position. This meant that enrichment data simulated using optimised parameters did not deviated from true values more than biases introduced by measurement errors.

(E) Normal probability plots of the residual errors from the best INS and CTRL solution. The departure from normality suggested some presence of systematic bias (poor model–data fit) and/or non-independent measurements.

(F) Illustrating the Monte-Carlo resampling process, whereby input data is repeatedly corrupted and solved for optimum solution to quantify the variance of the estimated parameters.

(G) Simulated distributions of the change (gradient) in standard deviations and medians as sample size is increased. Gradients were mostly near zero when sampling size was 30 or above. This confirms that resampling size of 50 was sufficient establish stable estimates of $v(t)$ and $c(t)$.

(H) Placement of knots from the 50 flux models for each condition. Knots are mostly away from the lower and upper bounds, suggesting that knot range determined in Panel C contains the optimum. Knots for CTRL were the densest around 12 minutes (0.2), which can be attributed to the transient effects caused by media exchange.

(I) Increasing the threshold for minimum error from 1% to 5%. The PCA plot shows that the re-optimised solutions (at 5% min error) was not very different compared our existing Monte-Carlo solutions and the original optimum solutions. At 5%, the best SSRs for both CTRL (385) and INS (384) were just under the chi-square cut-off (385 for CTRL, 469 for INS).

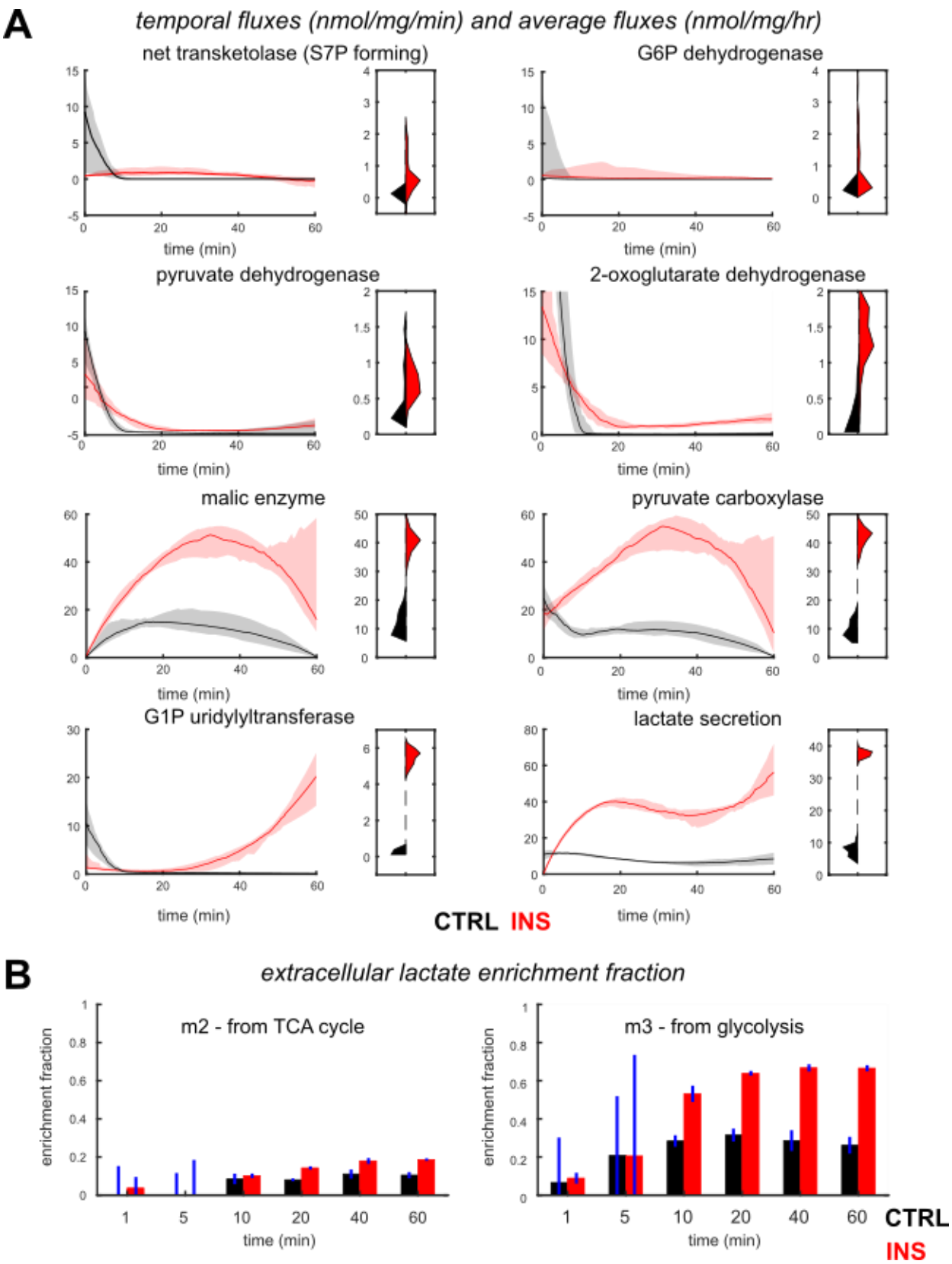


**Figure S4**. Additional information related to flux results. Related to Figure 4.

(A) Temporal and average fluxes of key pathway enzymes. Actual fluxes were shown, apart from the net transketolase flux (in the S7P forming direction). Line shows median flux, shaded area shows interquartile range from 50 Monte-Carlo replicates.

(B) Isotopologues of extracellular lactate, showing the increase in m+0, m+2 and m+3 fractions over time. The graphs highlight the increase in m+2 fraction in INS, which informed the high pyruvate-oxaloacetate-malate conversion. The increase in m+0 fraction in CTRL showed that lactate was predominant produced from non-glucose sources. Data are represented as mean ± 2×SEM of 3 biological replicates

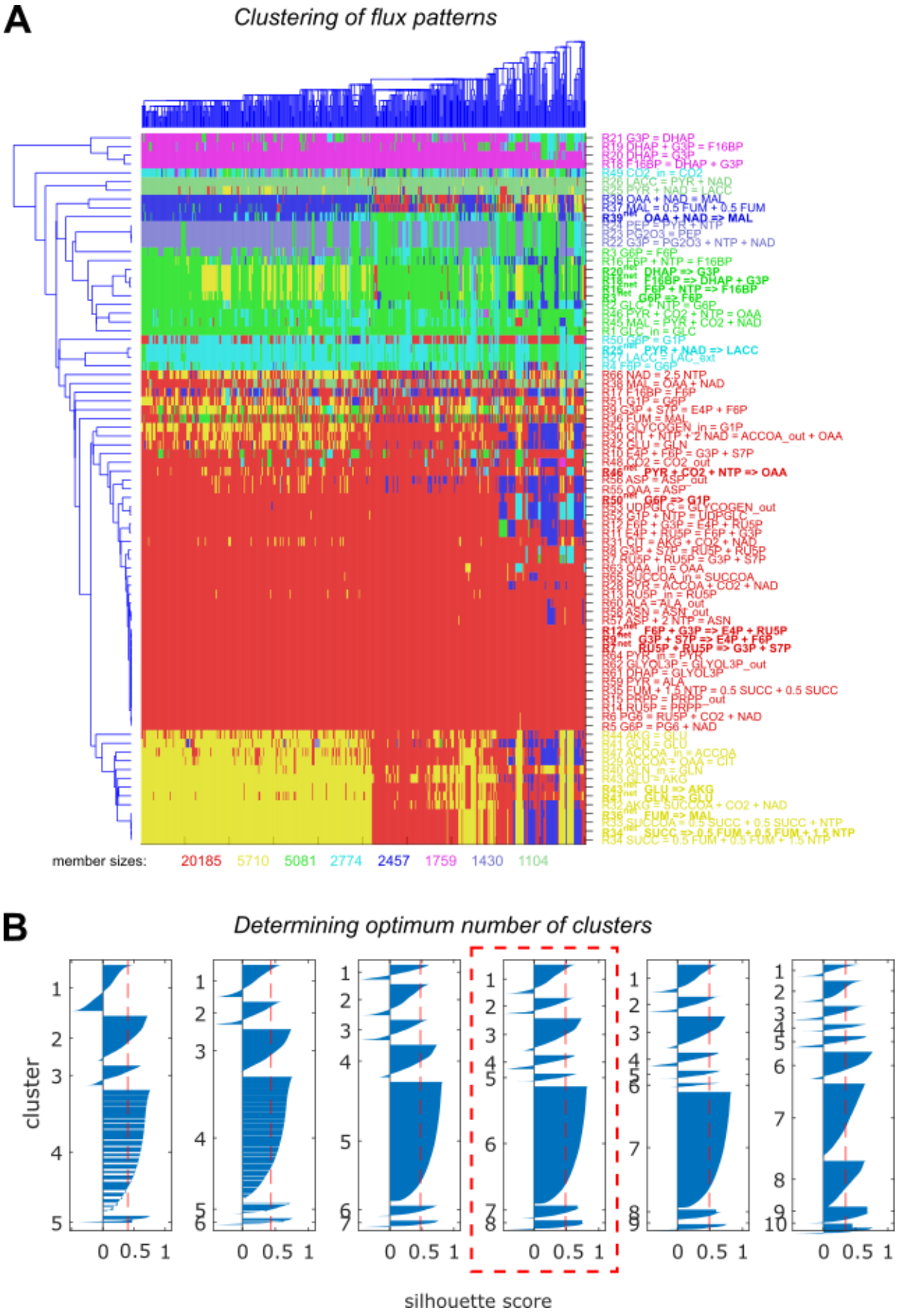


**Figure S5**. Clustering of temporal flux differences, Related to Figure 5.

(A) Heat map and clustergram show clustering information from the temporal flux differences between INS and CTRL. To generate flux differences, 500 random but non-redundant pairs were generated between the 50 flux models from both conditions; each model is paired exactly 10 times. Rows and columns were arranged based on the flux parameters (row) and INS-CTRL pairs (column) dendrograms. The colours used matches the eight clusters shown in Figure 5. The number of members in a cluster shown below heat map. A flux parameter can be associated to more than one cluster, but were assigned to a cluster (colour on the pathway map Figure 5B) based on majority. Net reactions are indicated (bold).

(B) Silhouette plots were used to determine optimum number of clusters based on squared Euclidean distance. Eight clusters produced the largest silhouette score.

## Transparent Methods

### Key resource table

| REAGENT or RESOURCE | SOURCE | IDENTIFIER |
|---|---|---|
| Chemicals, Peptides, and Recombinant Proteins | | |
| D-[UL-$^{13}C_6$]-glucose | Omicron Biochemicals | Cat# GLC-082; CAS 110187-42-3 |
| D-[$^{14}$C(U)]-glucose | Perkin Elmer | Cat# NEC042X001MC |
| Insulin from bovine pancreas | Sigma-Aldrich | Cat# I5500-1G; CAS 11070-73-8 |
| L-Methionine sulfone | Alfa Aesar | Cat# A17027; CAS 7314-32-1 |
| 2-(N-morpholino) ethanesulfonic acid | Sigma-Aldrich | Cat# 69889; CAS 145224-94-8 |
| D-Camphor-10-sulfonic acid | Wako | Cat# 037-01032; CAS 21791-94-6 |
| Critical Commercial Assays | | |
| Pierce BCA protein assay kit | Thermo | 23225 |
| Glycerol assay kit | Sigma | Cat# FG0100 |
| Glucose assay kit | Thermo | Cat# TR15221 |
| | | |
| Experimental Models: Cell Lines | | |
| Mouse: 3T3-L1 cells | Howard Green | - |
| Software and Algorithms | | |
| MATLAB | MathWorks | R2017b (9.3.0.713579) |
| Gurobi Optimizer | Gurobi Optimization | version 7.5, win64 |
| Other | | |
| | | |

### Contact for reagent and resource sharing

Further information and requests for resources and reagents should be directed to and will be fulfilled by the Lead Contact, Lake-Ee Quek (lake-ee.quek@sydney.edu.au).

### Experimental model and subject details

3T3-L1 cells

3T3-L1 fibroblasts were maintained as described previously (Fazakerley et al., 2015). Briefly, cells were cultured in Dulbecco's modified Eagle's medium (DMEM) supplemented with 10% (v/v) foetal bovine serum (Life Technologies) and 2 mM GlutaMAX (Life Technologies) at 37 °C with 10% CO2. Differentiation was induced at 100% confluence by addition of 250 nM dexamethasone, 350 nM insulin, 0.5 mM 3-isobutyl-1-methylxanthine and 400 nM biotin for 72 h (all of these reagents were from Sigma-Aldrich). Cells were then incubated in media containing 350 nM insulin for a further 72 h, and refreshed with naïve media every 2 d after. Adipocytes were used between days 9-12 after initiation of differentiation. We confirmed by visual inspection that at least 90% of the 3T3-L1 fibroblasts had differentiated into adipocytes prior to experiments. These cells were routinely tested for mycoplasma infection.

Unless otherwise specified, prior to insulin stimulation treatments, cells were washed three times with phosphate-buffered saline (PBS) and incubated in serum-starvation media: serum-free DMEM containing 0.2% (w/v) bovine serum albumin (BSA, Bovostar) and 2 mM GlutaMax.

### Method details

CE- or IC-coupled MS metabolomics

Following treatment in 6-well plates, cells were washed twice with cold 5% (w/v) mannitol on ice and lysed in 500 µl cold methanol containing 25 µM internal standards (L-methionine sulfone, 2-(N-morpholino) ethanesulfonic acid, D-camphor-10-sulfonic acid). Two wells (on separate plates) were scraped and pooled for each sample. Polar metabolites were extracted from 400 µl lysate with 200 µl water and 400 µl chloroform, passing 400 µl of the aqueous phase through a 5 kDa-cutoff spin-filter column (Millipore). The filtrate was dried using a vacuum centrifuge and resuspended in 25 µl water containing 200 µM reference compounds (3-aminopyrrolidine, trimesic acid) prior to analysis by MS.

All CE-TOFMS experiments were performed using an Agilent 1600 Capillary Electrophoresis system (Agilent technologies, Waldbronn, Germany), an Agilent G1969A LC/MSD TOF system (Agilent technologies, Santa Clara, CA), an Agilent 1100 series isocratic HPLC pump, a G1603A Agilent CE-MS adapter kit and a G1607A Agilent CE-electrospray ionization (ESI)-MS sprayer kit. In anionic metabolites analysis, ESI sprayer was replaced with a platinum needle instead of initial stainless steel needle (Soga et al., 2009), otherwise other conditions related to CE-ESI-MS sprayer were identical. For CE-MS system control and data acquisition, we used Agilent MassHunter software.

For anionic metabolome analysis, a COSMO(+) capillary (50 µm i.d. x 105 cm, Nacalai Tesque, Japan) filled with 50 mM ammonium acetate (pH 8.5) as the electrolyte was used (Soga et al., 2009). Before to the first use, a new capillary was flushed successively with the electrolyte, 50 mM acetic acid (pH 3.4), and then the electrolyte again for 10 min each. Before each run, the capillary was equilibrated by flushing with 50 mM acetic acid (pH 3.4) for 2 min and then with the electrolyte for 5 min. Sample was injected at 50 mbar for 30 s and a negative voltage of 30 kV was applied. The temperature of the capillary and sample tray was maintained at 20 °C and 4 °C, respectively. Ammonium acetate (5 mM) in 50% (v/v) methanol/water solution that contained 0.1 µM hexakis(2,2-difluoroethoxy)phosphazene was delivered as sheath liquid at 10 µL/min. ESI-TOFMS was operated in the negative ion mode, and the capillary voltage was set at 3.5 kV. The nitrogen nebulizer pressure was set at 10 psig and the nitrogen drying gas was set at 300 °C with a flow rate of 10 L/min. In TOFMS, the fragmentor, skimmer, and Oct RF voltages were set at 100, 50, and 200 V, respectively. Automatic recalibration of each acquired spectrum was performed using the masses of reference standards ([$^{13}$C isotopic ion of deprotonated acetate dimer (2CH3COOH−H)]−, m/z 120.03834 and ([hexakis(2,2-difluoroethoxy)phosphazene + deprotonated acetate(CH3COOH−H)]−, m/z 680.03554). Exact mass data were acquired at the rate of 1.5 cycles/s over a 50 to 1000 m/z range.

For cationic metabolome analysis, a fused-silica capillary (50 µm i.d. x 95 cm) filled with 1 M formic acid as the electrolyte was used (Soga and Heiger, 2000). A new capillary was flushed with the electrolyte for 20 min, and the capillary was equilibrated for 4 min by flushing with the electrolyte before each run. Sample solution was injected at 50 mbar for 3 s and a positive voltage of 30 kV was applied. The temperature of the capillary and sample tray was maintained at 20 °C and 4 °C, respectively. Methanol/water (50% v/v) containing 0.1 µM hexakis(2,2-difluoroethoxy)phosphazene was delivered as sheath liquid at 10 µL/min. ESI-TOFMS was operated in the positive ion mode, and the capillary voltage was set at 4 kV. The nitrogen nebulizer pressure was set at 10 psig and the nitrogen drying gas was set at 300 °C with a flow rate of 10 L/min. In TOFMS, the fragmentor, skimmer, and Oct RF voltages were set at 75, 50, and 125 V, respectively. Automatic recalibration of each acquired spectrum was performed using the masses of reference standards ([13C isotopic ion of protonated methanol dimer (2CH3OH+H)]+, m/z 66.06306) and ([hexakis(2,2-difluoroethoxy)phosphazene + H]+, m/z 622.02896). Exact mass data were acquired at the rate of 1.5 cycles/s over a 50 to 1000 m/z range.

Furthermore, analysis of glucose was performed by CE-QqQMS analysis as described previously with slight modifications (Klampfl and Buchberger, 2001). Briefly, an Agilent 6410 Triple Quad LC/MS system was used, with other instruments being identical to those for CE-TOFMS analysis. A fused-silica capillary (50 µm i.d. x 100 cm) filled with 300 mM diethylamine as the electrolyte was used. A new capillary was flushed with the electrolyte for 20 min, and the capillary was equilibrated for 5 min by flushing with the electrolyte before each run. Sample solution was injected at 50 mbar for 9 sec and a positive voltage of 20 kV was applied. The temperature of the capillary and sample tray was maintained at 20 °C and 4 °C, respectively. Isopropanol/water (80% v/v) containing 0.2% (v/v) diethylamine was delivered as sheath liquid at 4 µL/min. ESI-MS/MS was conducted in the negative mode, and the capillary voltage was set at 3.5 kV. The nitrogen nebuliser pressure was set at 7 psig and the nitrogen drying gas was set at 300 °C with a flow rate of 10 L/min. The MRM parameters for the internal standards (D-camphor-10-sulfonic acid, 2-(N-morpholino) ethanesulfonic acid) and glucose (unlabelled and labelled) are optimised using the optimiser function for the MassHunter software.

In addition, analysis of succinate and methylmalonate was performed by capillary ion-chromatography(IC)-coupled MS. Capillary IC-MS analysis were performed using a Dionex ICS-5000+ system equipped with a Q Exactive Orbitrap MS system (Thermo Fisher Scientific, San Jose, CA). Separations were performed on a Dionex IonPac AS11-HC-4 µm column (0.4 × 250 mm, 4 µm; Thermo Fisher Scientific) that was maintained at 35 °C, and the flow rate was 20 µl/min. The samples used for CE-MS were 10-times diluted with Milli-Q water and 0.4 µl were injected on column. The concentration gradient of KOH were as follows; 1 mM from 0 min to 2 min, 20 mM at 16 min, 100 mM at 35 min and then retained at the same concentration until 40 min, followed by decreasing to an initial concentration within 0.1 min and kept for 5 min. Total analysis time was 45.1 min. Isopropanol containing 0.1% (v/v) acetic acid was delivered as the sheath liquid at 5 µl/min.

Q Exactive mass spectrometer was operated under an ESI negative ion mode, and the spray voltage was set at 4.0 kV. The capillary temperature was 300 °C, sheath gas flow rate was 20, the auxiliary gas flow rate was 10, the sweep gas flow rate was 0, and the S-lens was 50 (arbitrary units). The parameters of the full

MS scan were as follows: resolution, 70,000; auto gain control target, 1×106; maximum ion injection time, 100 ms; scan range, 70 to 1,000 m/z. The instrument was calibrated at the beginning of each sequence using the calibration solution provided by the instrument manufacturer.

The raw data obtained by both CE-TOFMS and CE-QqQMS were processed using MasterHands (Hirayama et al., 2009; Sugimoto et al., 2010). The peaks were identified by matching m/z values and normalised migration times of corresponding authentic standard compounds. The raw data obtained by capillary IC-MS were analysed using TraceFinder (ver. 3.2) software. Summarised data provided (Data S1).

Extracellular lactate by LC-MS

20μL of adipocyte culture media was combined with 80μL of extraction buffer containing 1:1 (v/v) mixture of LC-MS grade methanol and acetonitrile and 0.25uM D-camphor-10-sulfonic acid internal standard. Mixture was vortexed and then centrifuged to pellet the precipitates. The supernatant was dried to completion using Eppendorf Vacufuge, resuspended in 20μL H2O and transferred into HPLC vials. LC-MS analysis was performed using an Agilent Infinity 1260 LC coupled to an AB Sciex QTRAP 5500 MS. LC separation was achieved on a Synergi 2.5 μm Hydro-RP column (Phenomenex, 2.1 mm I.D., 100 mm length) at ambient temperature using buffer A 95:5 (v/v) water:acetonitrile containing 10mM tributylamine and 15mM acetic acid (pH 4.9), and buffer B 100% acetonitrile. Injection volume was 2.5 μL. MS source temperature was set at 350 °C. MRMs were calibrated to include lactate isotopologues, and acquisition was performed with a 40 ms dwell time. Calibration standards were injected using the same set up. Raw data was extracted into text files using ProteoWizard. Peak alignment and integration were performed using in-house MATLAB scripts.

Glucose consumption assay

Following treatment, the plate of cells was chilled on ice and media was removed. Media was centrifuged at 2000 x g to remove debris and glucose content was measured using the glucose oxidase kit. Naïve treatment media was included as a control. Glucose consumption was determined by subtracting the glucose content of the conditioned media from the naïve media.

Lactate secretion assay

For media measurements, following incubation, the plate was placed on ice and an aliquot of media was removed. The media was assayed for lactate content as described previously (Prabhu et al., 2013). Briefly, an aliquot was diluted in water (100 µl total) and incubated with 100 µl assay buffer (1 M glycine pH 9.2, 0.4 M hydrazine in 1.2 M NaOH, and 2.5 mM EDTA, adjusted to pH 9.2 with NaOH prior to addition of 4 mM NAD+ and 2 U/ml lactate dehydrogenase). Following incubation at room temperature for at least 1 h, the absorbance of NADH was measured at 340 nm. The media was assayed for glucose content using the glucose oxidase kit (Thermo Fisher Scientific) (Krycer et al., 2017). In both assays, naïve treatment media was included as a control.

Glycogen assay

Following treatment, glycogen was harvested as described previously (Thompson et al., 2000; Van Handel, 1965). Briefly, the plate of cells were quenched by washing thrice with ice-cold PBS, after which the plate was aspirated dry and frozen at -20 °C. The plate was thawed on ice and each well was scraped in 200 µl of 1 M KOH. Following the addition of 75 µl saturated Na2SO4 and 1.8 ml ethanol, lysates were vortexed briefly and centrifuged at 16000 x g and 4 °C for 15 min. The supernatant was removed and pellet resuspended in 180 µl water using the ThermoMixer C (Eppendorf) at 1000 rpm and 70 °C. Ethanol (1.62 ml) was added, the mixture was vortexed briefly and centrifuged at 16000 x g and 4 °C for 15 min. The supernatant was removed and the pellet was dissolved in 400 µl water using the ThermoMixer C (Eppendorf) at 1000 rpm and 70 °C. Samples were assessed for radioactivity by liquid scintillation counting.

Radiolabelling experiments

Cells were initially serum-starved for at least 1.5 h in DMEM buffered by HEPES (20 mM, pH 7.4), supplemented with 0.2% (w/v) bovine serum albumin, 25 mM glucose, 1 mM GlutaMAX, and 1 mM glutamine. Cells were then incubated in the same media, except supplemented with 10 mM glucose and [U-14C]-glucose (1 µCi/ml). A lower glucose concentration was used to increase the specific activity of the radiolabelled glucose. Cells were incubated at 37 °C in a non-CO2 incubator for these experiments.

For glucose oxidation experiments, cells were assayed as described previously (Krycer et al., 2018). Briefly, immediately upon addition of radiolabelled media and insulin (100 nM) treatment, gas-traps containing NaOH were installed and plates were sealed. Following incubation, the contents of each well was acidified with perchloric acid and plates were re-sealed. After at least 1 h, the NaOH in the gas-traps was assayed for radioactivity by liquid scintillation counting. Cell-free controls were performed to account for any cell-independent, tracer batch-dependent changes in signal.

For lipogenesis experiments, cells were assayed as described previously (Krycer et al., 2018). Following incubation with radiolabelled medium, cells were washed thrice with ice-cold PBS and plates were frozen dry at -30 °C. Plates were then thawed and cells were scraped in ice-cold 0.6% (w/v) NaCl. An aliquot was solubilised with addition of 0.1 vol of 10% (w/v) SDS and protein content was quantified by the BCA assay. The lipids were extracted from the remainder using CHCl3:MeOH (2:1)(Folch et al., 1957). An aliquot was evaporated to dryness and radioactivity was assayed by liquid scintillation counting. The remainder was evaporated to dryness and saponified: first, 1.5 ml of 1 M KOH was added and samples were incubated at 70 °C for 15 min. 1 ml EtOH was then added and samples were incubated at 70 °C for 2 h. Following saponification, 0.25 ml of 9 M H2SO4 was added, and free lipids were isolated by 3 rounds of petroleum ether extraction (Stansbie et al., 1976). Lipids were then washed with 2.5 ml water to remove any contaminating aqueous metabolites, involving mixing with water, freezing and decanting the upper (organic) phase. The organic fraction was then evaporated to dryness and radioactivity was assayed by liquid scintillation counting. The saponified sample provided an estimate of glucose incorporation into fatty acids, whereas the difference between the saponified and unsaponified samples provided an estimate of glucose incorporation into the glycerol backbone of triacylglycerides. Naïve 0.6% (w/v) NaCl was processed in parallel to account for any background signal.

B-spline construction

A B-spline curve of $n^{th}$ order with clamped ends is constructed from linear combination of $j \geq n$ pieces of polynomials of degree < $n$ (i.e., constant $n$ =1, linear $n$ = 2, quadratic $n$ = 3, cubic $n$ = 4) (Equation S1). The polynomial pieces (Figure S1H), or basis functions ($N_{i,n-1}$), are derived from the Cox-de Boor recursion formula (Equation S2, Figure S1E). There are $j + n$ knots (or breakpoints), and $j – n$ internal knots. Internal knots control the span of the polynomial pieces when $j > n$. $t_1, t_2, \ldots, t_{j+n}$ are the series of knots, and can be placed over the domain [0, 1] or scaled to real-time (e.g., 60 minutes) (Figures S1G). A clamped-ends B-spline curve passes through the two flanking CP values, $CP_1$ and $CP_j$. This is achieved using knot multiplicity, where $t_1 = t_2 = \ldots t_n$ and $t_{j+1} = t_{j+2} = \ldots = t_{j+n}$ (Figure S1F).

$$B(x) = \sum_{i=1}^{j}\left(CP_i \cdot N_{i,n-1}\right) \qquad \text{Equation S1}$$

$$N_{i,0}(x) = \begin{cases} 1 & if\ t_i \leq x < t_{i+1} \\ 0 & otherwise \end{cases}$$

$$N_{i,k}(x) = \frac{x-t_i}{t_{i+k}-t_i} N_{i,k-1}(x) + \frac{t_{i+k+1}-x}{t_{i+k+1}-t_{i+1}} N_{i+1,k-1}(x) \qquad \text{Equation S2}$$

$$k = 0,1,\cdots,n-1$$

$$i = 1,2,\cdots,j+n-1$$

$$t = [t_1 \quad \cdots \quad t_{j+n}]$$

Knot position define the local support of a $CP$ (Figure S1H); it dictates the segment of the spline where a particular CP has non-zero contributions. More importantly, knot position must be specified upfront such that $B(x)$ can be expressed as a linear function of $x$.

The same $CP$ values are used to integrated B-splines (Equation S3). The new basis function ($N_{i,n}$) is generated as usual (using Equation S2), with the order increased by one and using $t^{int}$. The integral form $N_{i,n}^{int}$ is generated by scaling $N_{i,n}$ using an upper triangular matrix with repeating row values according to the knot span (Equation S4). Clamped ends are maintained by duplicating the flanking knots ($t_1 = 0$, $t_{j+n} = 1$). The initial value is fixed to zero.

$$\int B(x)dx = \sum_{i=1}^{j+1}\left(CP_i^{int} \cdot N_{i,n}^{int}\right) \qquad \text{Equation S3}$$

where $CP_i^{int} = [0 \quad CP_1 \quad \cdots \quad CP_j]$
$t^{int} = [0 \quad t \quad 1]$

$$\begin{bmatrix} N_{1,n}^{int} \\ N_{2,n}^{int} \\ \vdots \\ N_{j+1,n}^{int} \end{bmatrix} = \frac{1}{n} \cdot \begin{bmatrix} t_{1+n}^{int} - t_1^{int} & t_{1+n}^{int} - t_1^{int} & t_{1+n}^{int} - t_1^{int} & t_{1+n}^{int} - t_1^{int} \\ 0 & t_{2+n}^{int} - t_2^{int} & t_{2+n}^{int} - t_2^{int} & t_{2+n}^{int} - t_2^{int} \\ 0 & 0 & \ddots & \vdots \\ 0 & 0 & 0 & t_{j+1+n}^{int} - t_{j+1}^{int} \end{bmatrix} \cdot \begin{bmatrix} N_{1,n} \\ N_{2,n} \\ \vdots \\ N_{j+1,n} \end{bmatrix} \qquad \text{Equation S4}$$

Similarly, the derivative of B-splines can be calculated using the same CP values (Equation S5). The new basis function ($N_{i,n-2}$) is generated as usual (using Equation S2), with the order decreased by one and using $t^{der}$. Clamped ends are maintained by eliminating the flanking knots $t_1$ and $t_{j+n}$.

$$\frac{d}{dx}B(x) = \sum_{i=1}^{j}\left(CP_i \cdot N_{i,n-2}^{der}\right) \qquad \text{Equation S5}$$

where $t^{der} = [t_2 \quad \cdots \quad t_{j+n-1}]$

$$\begin{bmatrix} N_{1,n-2}^{der} \\ N_{2,n-2}^{der} \\ \vdots \\ N_{j,n-2}^{der} \end{bmatrix} = (n-1) \cdot \begin{bmatrix} -(t_{1+n-1}^{der} - t_1^{der})^{-1} & 0 & 0 & 0 \\ (t_{1+n-1}^{der} - t_1^{der})^{-1} & -(t_{2+n-1}^{der} - t_2^{der})^{-1} & 0 & 0 \\ 0 & (t_{2+n-1}^{der} - t_2^{der})^{-1} & \ddots & \vdots \\ 0 & 0 & 0 & \left(t_{i+n-1}^{der} - t_i^{der}\right)^{-1} \end{bmatrix} \cdot \begin{bmatrix} N_{1,n-2} \\ N_{2,n-2} \\ \vdots \\ N_{j,n-2} \end{bmatrix}$$ Equation S6

B-splines fluxes and concentrations

B-splines support the generation of dynamic fluxes in any shape or form. The prerequisite for smooth fluxes sets the order of the B-spline to be 3 (quadratic) or above. More importantly, fluxes were made to satisfy mass conservation constraints at the metabolite level by imposing metabolite balancing and constraining metabolite abundance to be non-zero ($c(t) > 0$). Metabolite balancing (mass conservation) is enforced by the stoichiometric matrix *S*.

Each flux is independently parameterised, but has the same knot position. There are *j* free parameters for each flux (since there are *j* pieces of polynomials), where $j \geq n$. $v(t)$ and $c(t)$ for a reaction network with *R* reactions and *Q* metabolites can be expressed in matrix form (Equation S7 and Equation S8). To impose the inequality constraint $c(t) > 0$, the time slices from Equation S6 are assembled into a single large constraint matrix (Equation S9).

$$v(t) = \begin{bmatrix} CP_{1,1} & \cdots & CP_{1,j} \\ \vdots & \ddots & \vdots \\ CP_{R,1} & \cdots & CP_{R,j} \end{bmatrix} \cdot \begin{bmatrix} N_{1,n-1} \\ \vdots \\ N_{j,n-1} \end{bmatrix}$$ Equation S7

$$c(t) = \begin{bmatrix} S_{1,1} & \cdots & S_{1,R} \\ \vdots & \ddots & \vdots \\ S_{Q,1} & \cdots & S_{Q,R} \end{bmatrix} \cdot \begin{bmatrix} 0 & CP_{1,1} & \cdots & CP_{1,j} \\ \vdots & \vdots & \ddots & \vdots \\ 0 & CP_{R,1} & \cdots & CP_{R,j} \end{bmatrix} \cdot \begin{bmatrix} \int N_{1,n} \\ \vdots \\ \int N_{j+1,n} \end{bmatrix} + \begin{bmatrix} c_{0,1} & \cdots & c_{0,1} \\ \vdots & \ddots & \vdots \\ c_{0,Q} & \cdots & c_{0,Q} \end{bmatrix}$$ Equation S8

where $S_{q,r}$ is the stoichiometry of metabolite *q* in reaction *r*, and $c_{0,q}$ is the initial abundance of metabolite *q*.

$$C = \begin{bmatrix} c(t=0) \\ \vdots \\ c(t=T) \end{bmatrix} = \begin{bmatrix} I & S \cdot \int N_n(t=0) \\ \vdots & \vdots \\ I & S \cdot \int N_n(t=T) \end{bmatrix} \cdot \begin{bmatrix} c_o \\ CP^v \end{bmatrix}$$ Equation S9

where $CP^v$ is the *CP* matrix (*j* columns × *R* rows) in vector form and $\int N_n$ is the corresponding basis function matrix.

Verifying accuracy of SBR EMU modelling using a toy model

The EMU framework provides a model system to track how atoms propagate through a network (Antoniewicz et al., 2007). A network of continuous stirred tank reactors (CSTR) is the most accurate abstraction of metabolite conversions (Figure 2B). Using the Sequencing Batch Reactors (SBR) approach, the continuous propagation of EMUs is modelled as discrete steps, which each step comprised of "filling" a tank with pre-existing content with new contents through one or more channels, followed by "mixing" (Figure 3C). It models the continuous conversion of cellular metabolites as a network of batch reactors. SBR is an explicit numerical approach. To ensure that estimate parameters are accurate within tolerance (as numerical methods incur truncation error), we compared this new approach against MATLAB's solver for ordinary differential equations, *ODE45 and ODE15s*. Note that $c(t)$ is calculated analytically from $v(t)$ using B-spline integration, and not by a numerical approach.

An 8-reaction toy model representing the TCA cycle was created, with pyruvate and 2-oxoglutarate as the main input and output respectively (Figure S2E, Supplemental Information Data S1). The toy model allows the production of 2-oxoglutarate by pyruvate carboxylase. Hypothetical (reference) dynamic fluxes were generated using order 3 B-spline and four fixed internal knots; initial concentrations were arbitrarily set to 100. Flux and metabolite units are arbitrary. Pyruvate was modelled as uniformly labelled. Metabolite isotopologues were simulated for six metabolites (pyruvate, acetyl-CoA, citrate, oxaloacetate, 2-oxoglutarate, $CO_2$) sampled across 10 timepoints (1, 5, 10, 15, 20, 25, 30, 40, 50 and 60 min). *ODE45* was used to generate the metabolite data from the reference fluxes. The synthetic data was then corrupted with one standard deviation Gaussian noise. The error term was arbitrarily set to 5, i.e., approximately 5% relative error. Finally, the "experimental" data was subjected to optimisation for fluxes using MATLAB's ODE solvers and the SBR algorithm.

Numerical integration of Equation 3 was performed using *ODE45*, ODE15s with the analytical Jacobian matrix, and our SBR algorithm. With *ODE15s*, the analytical Jacobian matrix (*J*) was additionally provided, whereby $J = \frac{df}{dX}$ with *f* representing Equation 3 (i.e., $f = \frac{dX}{dt}$). The ODE solvers call for adaptive time steps, hence our B-spline algorithm was modified such that the basis functions are modified accordingly by the solvers. MATLAB's default error tolerance for *ODE45* was used.

For our method, 6 different uniform step sizes were tested: 5, 2, 1, 0.5, 0.2 and 0.1 minute, thus producing 14, 35, 61, 121, 301 and 601 SBR steps (Figure 2F). For the 2-minute step size, additional steps at 1, 5, 15 and 25 were added to match the steps with the sampling timepoints. We recorded the optimisation run time (up to 100 repeats). We used unweighted Manhattan distance to quantify the accuracy of the estimated parameters relative to the reference solution (Figure 2F).

The reference solution was generated from the toy model by first creating an artificial set of solution, simulating the EMUs and corrupting them to make them resemble experimental data. Optimisations were repeated 200 times for the ODE solvers, and 100 times for each SBR configuration. The deviations of the optimised solutions from the synthetic true solution were reported as Manhattan distances. The best SSR value was 76; Optimisations returning SSR above 100 were treated as failed optimisations. The optimisations were timed from start to finish.

Metabolic model construction

The metabolic model contained reactions needed to connect labelled media glucose to enriched metabolites. 27 metabolite isotopologues (units: pmol/mg protein) were chosen for 13C-DMFA because they were enriched (Data S1). Classical mammalian pathways were included, namely glycolysis, pentose-phosphate pathway (PPP), TCA cycle, glutaminolysis and anapleurosis via pyruvate carboxylase (PC) (Figures 3E and 4A). Known insulin-stimulated outputs of adipocyte were added, such as lipogenic acetyl-CoA, glycerol 3-phosphate, glycogen and lactate, to draw glucose through the network. The synthesis of alanine, aspartate, glutamate, glutamine, asparagine and phosphoribosyl pyrophosphate were included as potential sinks because these metabolites were enriched. Metabolite balance included ATP and redox (NAD and NADP lumped as one) to ensure that their consumption did not exceed supply. Oxidative phosphorylation was added to permit generation of ATP from redox surplus. Glycogen pool was modelled as glucose monomers, but influx glycogen is treated as unlabelled (i.e., endogenous glycogen pool >> synthesis). Atom transitions were collated from published works and KEGG pathway maps (Kanehisa et al., 2006; Suthers et al., 2007).

Additional substrates sources were introduced, namely acetyl-CoA, succinyl-CoA, glutamine, oxaloacetate, pyruvate, glycogen and ribulose 5-phosphate, to account for active catabolism of non-glucose substrates. These precursors can be derived from amino acid catabolism (e.g., branch chain amino acids), transamination reactions, glycogenolysis and nucleotide turnover. The uptake of unlabelled CO2 was added to account for bicarbonate exchange. The final model is a single-compartment model with 66 reactions and 34 internal metabolites (Supplemental Information Data S1).

Most metabolites in the model were associated with data, but a few were without. These metabolites were glyceraldehyde-3-phosphate (G3P), pyruvate, oxaloacetate, CO2 and erythrose-4-phosphate (E4P). During modelling, the abundance of these metabolites were not constrained.

Below are the metabolite abbreviations used in the adipocyte model:

| Abbreviation | Name | Abbreviation | Name |
|---|---|---|---|
| ACCOA | acetyl-CoA | GLYCOGEN | glycogen |
| ACCOA_out | lipogenic acetyl-CoA | GLYOL3P | glycerol 3-phosphate |
| AKG | 2-oxoglutarate / alpha-ketoglutarate | LACC | lactate (cellular) |
| ALA | alanine | LAC_ext | lactate (extracellular) |
| ASN | asparagine | MAL | malate |
| ASP | aspartate | NAD | NADH / NADPH |
| CIT | citrate | NTP | ATP (nucleotide triphosphate) |
| CO2 | carbon dioxide | OAA | oxaloacetate |
| DHAP | dihydroxyacetone phosphate / glycerone phosphate | PEP | phosphoenolpyruvate |
| E4P | erythrose 4-phosphate | PG2O3 | 2-phosphoglycerate & 3-phosphoglycerate |
| F16BP | fructose 1,6-bisphosphate | PG6 | 6-phosphogluconate |
| F6P | fructose 6-phosphate | PRPP | phosphoribosyl pyrophosphate |

| | | | |
|---|---|---|---|
| FUM | fumarate | PYR | pyruvate |
| G1P | glucose 1-phosphate | RU5P | ribose 5-phosphate / ribulose 5-phosphate / xylulose 5-phosphate |
| G3P | glyceraldehyde 3-phosphate | S7P | sedoheptulose 7-phosphate |
| G6P | glucose 6-phosphate | SUCC | succinate |
| GLC | glucose | SUCCOA | succinyl-CoA |
| GLN | glutamine | UDPGLC | UDP-glucose |
| GLU | glutamate | | |

Calibrating B-spline order and knots

To address the concern of overfitting, we tested B-spline orders of 1 to 3, in combination with up to three internal knots (Figure 3C). Using Akaike Information Criterion (AIC) to penalise excessive parameters, we chose the configuration O3K1 (order of 3, one internal knot) as it gave the lowest AIC score for INS. For CTRL, this configuration ranked intermediate; O2K3 gave the lowest AIC score, with knots placed early (< 5 minute).

SSRs were most sensitive to the placement of the first knot according to the cubic envelope demarcating knots with lowest SSRs as a function of time (Figure 3C). SSRs for higher order B-splines, which have a greater capacity for curvatures, were less sensitive to knot placement. As knot position are estimated parameters as well, our strategy forward was thus to have the Monte-Carlo method sample knots within a reasonable interval narrowed by prototyping solutions. We used boundaries defined by knots within the 20$^{th}$ percentile (Figure S3C).

SBR time step calibration and validation

There is a speed and accuracy trade-off when integrating numerically. To strike a balance we ran large (>1000) random permutations of uniform and non-uniform time steps, ranging from 20 to 30,000 steps between a pair of sampling points. The aim is to choose the configuration with the least number of steps that still yielded SSRs within a given cut-off (Figure 2H).

This calibration was performed using a synthetic data generated from prototyping INS optimisations. The INS set was used, rather than CTRL, because we expect a greater dynamics in this dataset and hence will require smaller time steps. For prototyping, large uniform 20-step between sample points was arbitrarily chosen. This configuration was quick to yield initial feasible solutions from random starts and near-optimum solutions, but caused the overestimation of $\nu(t)$ due to a reduced rate of label propagation.

For each set of the time step configuration (generated by random and supervised/manual permutations), weighted Euclidean (residual) distance was used to quantify the deviation of simulated data from the reference (Figure 3D). We elected for a residual distance cut-off of 500. This value is comparable to the $\chi^2$ critical value and the median residual distance observed during data corruption with one standard deviation Gaussian noise (Figure 2H). We chose the least total number of steps that satisfy this cut-off, which was [500, 400, 200, 75, 75, 50]. At this step-size configuration, the computational speed was 10-fold slower than prototyping, i.e., 10 times more steps. Thus, we could toggle computational speeds between fast/coarse prototyping and slow/accurate result generation.

We verified that the optimised SBR time step configuration was adequate by repeating the above procedure using the final optimum solution from INS (Figure 3E). The residual distance (about 100) was less than the residual error caused by measurement noise (SSR = 480) (Figure 2H). Note that prototyping and final solutions are different because EMUs calculated using the prototyping (coarse) time step is less accurate. Here, the reference data was generated using a uniform 50,000-step. The optimised configuration produced a residual distance slightly over 100, and was located near the lower envelope (Figure 3E). At 30,000-step, the residual value less than 0.001 (c.f., actual SSRs were >1000), confirming that the reference generated at 50,000-step was sufficiently precise.

Since the SBR time step configuration of [500, 400, 200, 75, 75, 50] was calibrated heuristically, we needed to validate the accuracy of the approach. Hence, we took the final solutions from CTRL and INS generated from Monte-Carlo resampling and simulated the EMUs using *ODE15s* (with Jacobian). These simulated EMUs were then compared against EMUs generated using the existing time step configuration (termed SBRx1), and with step sizes density increased by 2.5- and 20-fold (SBRx2.5, SBRx20) to roughly match computation times of ODE15s with and without Jacobian, respectively. The ratios of steps between sampling timepoints were maintained. Note that *ODE45* was 3- to 4-fold faster than *ODE15s* without Jacobian, but only simulations from ODE15s were shown (Figure 2G). Weighted error was calculated using the same

objective function (Equation 6), except that reference data ($data_{mea}$) was taken from EMUs simulated by *ODE15s* with Jacobian. Runtime was determined based on the time required compute the objective function using the respective approaches.

MATLAB optimisation

Optimisation is performed using MATLAB non-linear constrained programming solver *fmincon*. Essentially, we are "guessing" *CP* and $c_0$ to minimize the sum of squared residuals (SSR) without depleting metabolite pools completely, i.e., $c(t) > 0$. Bi-directional reactions are provided in the forward and backward pairs, rendering all fluxes positive $v(t) > 0$. Solver implementation used Equation 1, 2 and 5, with Equation S9 applied as a linear inequality constraint matrix. Equation 3 is customised to match input data (Figure S2A). Endogenous metabolites were assumed to be naturally labelled at $t = 0$.

To improve the optimisation procedure, the fitted parameters *CP* and $c_0$ were given sufficiently large linear bounds and then scaled to [0,1]. Fluxes were constrained to be within 10 and $1\times10^5$ pmol/mg protein/min by setting these two values as the lower and upper bounds of *CP*, since $v(t)$ is contained within the convex hull of the control polygon defined by *CPs* (i.e., $\min(CP) \leq v(t) \leq \max(CP)$) (Figure 1F). Initial metabolite concentrations were constrained to the range $\left[\min(c_q) - 4\sigma, \max(c_q) + 4\sigma\right]$ pmol/mg protein, or [0.01, $1\times10^4$] pmol/mg protein for metabolites without data.

Customising 13C-DMFA objective function

Equation 6 is a generalised form of the least-square objective function . Figure S2A explains how the experimental data ($data_{exp}$) and the simulated data ($data_{sim}$) vectors were generated and put together in the objective function. Mainly, both measured and simulated data must represent the same entity, particularly when input data is heterogeneous and contains missing values (Figure S2B). Missing values are comprised of incomplete mass isotopologue distributions. In addition to isotopologues of intracellular metabolites, the input data was also included extracellular lactate time course, and radiolabelled data of glycogen and fatty acids at 60 minutes. Extracellular lactate was treated in the same manner as intracellular data. Glycogen and lipogenic acetyl-CoA were treated as accumulating pools.

The raw data, acquired as isotopologue concentrations, was first converted into aggregated concentrations and relative mass fractions before being subjected to optimisation (Figure S2A). Missing values were prevalent among the dataset; only 150 out of 324 sets were complete (Figure S2B). To ensure consistency, both measured and simulated sets used aggregated concentrations and relative mass fractions calculated from non-zero isotopologue entries in the measured set. The correction for natural isotopic interference, based on user-specific ion formula, is thus made prior to normalisation using aggregated concentrations. Overall, this treatment avoids imposing zero constraints on missing values.

The simulated EMUs, GLYCOGEN_out and ACCOA_out, at t = 60 minute were converted into units consistent with the outputs of radiolabelled assays (pCmol glucose/mg protein) (Figure S2A). The conversion involves mapping EMUs to the elementary components of the labelled substrate; glucose in this case because 14C-glucose was used. For glycogen, the main elementary components are fully labelled or unlabelled glucose. Minor components, comprised of single, double and triple labelled hexose backbone generated from reversible glycolysis and PP pathway, were omitted here. For acetyl-CoA, we used the complete set of elementary components because it has only 2 carbons. The transformation matrix *T* weighs the direct contribution of substrate to an EMU, and is generated based on the mappings of the elementary components to the input substrate. The columns of *T* contain mass isotopologue distribution of the elementary components calculated based on enrichment purity of the substrate. Illustrated in Figure S2A, *T* specifies the one-step conversion of $^{13}$C-glucose and naturally-labelled glucose carbons into GLYCOGEN_out and ACCOA_out EMUs. Hence, by inverting *T*, the number of labelled glucose carbon (pCmol glucose/mg protein) contained in glycogen and lipogenic acetyl-CoA isotopologues can be calculated.

Note that during data fitting, glucose carbon was assumed to be 99% enriched, whereas endogenous metabolites and other input substrates were assumed to be 1.07% enriched.

During prototyping, we discovered that the model could not recapitulate the unlabelled (m0) fractions, which were unexpectedly high and stable (Figure S3A). For CTRL, although unlabelled glucose level has plateaued at $\leq$ 15%, downstream metabolites generally remained ≥ 40% unlabelled. This discrepancy suggested that glucose did not fully displace endogenous metabolites due to non-ideal mixing, and/or the unlabelled pools were sustained by influx of non-glucose sources. The nuisance parameters for stagnant partition were thus incorporated when calculating the objective value. This ad hoc modification compensates for metabolites that have persistently unlabelled fractions that could not be explained by uptakes of unlabelled substrates. These parameters are expressed in concentration terms (pmol/mg protein), are converted into isotopologue concentrations assuming metabolites in the stagnant partition are naturally enriched (Figure S2A). Note that $c(t)$ calculated by Equation 2 represents the active partition.

Measurement variances used for error weighting were re-estimated by Monte-Carlo resampling (10000 iterations). We used the standard deviations (of triplicates, with Bessel's correction) of the isotopologue concentrations. The variance for concentration was then calculated after summing up the isotopologues. The variance of enrichment fractions was calculated after converting individual set of isotopologues, at each iteration, into mass fractions. We imposed a blanket minimum error of 0.01 to the mass fractions, which enlarged 61% of the error terms. This minimum error reflects isobaric interferences incurred during MS-acquisitions (Buescher et al., 2015). Also, since mass fractions sum up to 1, one redundant data point for each isotopologue was omitted from SSR calculations; the largest mass was chosen (Figure S2A). Measurements were assumed to be independent, thus the *error weight* matrix in Equation 6 is a diagonal matrix containing re-estimated measurement variance.

Optimisation workflow

The proposed optimisation workflow attempts to balance computational demand and adequate determination of the optimisation solutions. With a total of 329 free parameters (66 fluxes $\times$ 4 CPs each, 37 initial concentrations, 28 stagnant pools), irregular optimisation convergence is a significant issue, evident from the vertical spread of SSRs (Figure 3C). Mean computation times using coarse (prototyping) and fine (final) step sizes were about 6 and 40 hours respectively. Furthermore, optimum knot position is determined by repeated sampling during optimisation. As optimisations were performed on high performance computing clusters, the actual workflow carried out was performed in batches.

First, optimisations were performed on the original dataset to narrow down the range of knot position used subsequently during Monte-Carlo optimisation. 100 optimisations were performed on each dataset, using the prototyping time step. Non-optimal knot placement only elevated SSR marginally compared to the variability of SSRs values caused by poor optimisation termination. Thus, by narrow down the knot range beforehand (Figure S3C), we could dedicate more computation time towards estimating *CP*s and $c_0$.

Secondly, we used a two-stage optimisation procedure. Each optimisation is initialised and solved using the prototyping step size (uniform 20-step). The solution produced is then subjected to another round of optimisation using the fine step size configuration [500, 400, 200, 75, 75, 50]. For the original (uncorrupted) dataset, we could afford to progress every "coarse" solution into the "fine" optimisation stage. For Monte-Carlo optimisations using corrupted datasets (50 sets per condition), we performed multi-start optimisation 20 times for each set using the prototyping step size, and only the best solution from each set proceeded to the next optimisation stage using the fine step size configuration. The 20 times multi-start optimisation is required to sample for an optimum knot position specific to that corrupted set. Based on past optimisation success rates (Figure S3D), 20 iterations appeared to be adequate.

The minimum SSR for the INS and CTRL datasets obtained during final optimisations were 1603 and 1167 respectively. Both exceeded the critical $\chi^2$ values of 469 and 385 at 5% significance. However, by visual inspection our model reproduced the majority of the data points for both INS and CTRL, and errors were not associated to any specific pathway (Supplemental Information Data S1). We eliminated the possibility of unsuccessful optimisation convergence by challenging our workflow with a corrupted synthetic dataset. Knots were placed close to the true solutions and the SSRs returned (INS:546, CTRL:448) were consistent with both the residuals caused by data corruption and the $\chi^2$ cut-off (Figure S3D). This eliminated poor optimisation termination as a cause of the high SSRs. As the source of the high residuals was not clear cut, we proceeded without making any further modification to the data.

**Quantification and statistical analysis**

Time steps used during results analyses

Irregular step size was using during optimisation to generate the final temporal flux models. For our analyses, we took the optimised solutions and simulated flux and metabolite data with step size of 0.05 minute.

PCA plot

A PCA plot was used to show changes in metabolite abundances caused by media exchange. Z-scores were generated from the total metabolite abundances of central carbon metabolites (Data S1). MATLAB Principal Component Analysis function *pca* was used on the z-scores. MATLAB's default was used. Principal components were calculated based on 8 dataset: CTRL-10, CTRL-10', CTRL-60, CTRL-60', INS-10, INS-10', INS-60 and INS-60' (apostrophe represent data from media exchange experiment). INS-1, INS-5, INS-20 and INS-40 were subsequently plotted after converting them using the same orthogonal transformation.

Knots lower envelope

A cubic function was generated to help visualise the lower boundary of knots, which were scattered in the time (x-axis) and SSR (y-axis) domain (Fig. 2c). The function is placed as close as possible to the lowest

knots, thus capturing the how the minimum SSRs vary across time. To accomplish this, quadratic programming was performed in MATLAB using Gurobi Optimizer. The least-square distance of the cubic function from all knots was minimised, but at the same time the cubic function is constrained to be under all the knots.

Average fluxes

To summarise temporal fluxes, we integrated the area-under-the-curve (AUC) using B-spline integration (Equation S4). B-spline integration is analytically precise and not affected by time step configuration.

$$AUC_{flux} = \int v(t)dt = [0 \quad CP] \cdot \int N \qquad \text{Equation S10}$$

Average fluxes reported in Figures 4B and S4A were generated by integrating between t = 10 and t = 60, then divided the area by the integration time (50 minutes). The first 10 minutes were omitted due to confounding effects from media exchange.

To calculate the total amount of substrates entered the system (Figure 6D), we calculated $AUC_{flux}$ by integrating between t = 0 and t = 60, and then multiplied by metabolites' value by the number of carbons. Fluxes reported in Fig. 6f were also calculated by integrating between t = 0 and t = 60.

The same procedure can be applied to calculate average metabolite concentrations (for residence time calculations)

$$AUC_{concentration} = \int c(t)dt = [0 \quad 0 \quad CP] \cdot \iint N \qquad \text{Equation S11}$$

Substrate redistribution

The carbon contribution of substrates was simulated one substrate at a time. To examine glucose, extracellular glucose enrichment was modified such that all glucose carbon is 100% labelled, and at the same time, the enrichments of all other input substrates and endogenous metabolites were modified to be 100% unlabelled. EMUs were then simulated using the temporal flux models for each condition. Finally, the redistribution of that substrate is calculated by multiplying the EMUs (in fraction) at t = 60 with the corresponding abundance and number of carbon (Figures 6A and 6C). Here, the time step used during these simulations was the same configuration as the final optimisation. Estimates for glucose distribution provided (Data S1).

To generate the composite fractions (Figure 6C), the procedure above was repeated for CO2, glutamine, glycogen, pyruvate and acetyl-CoA. The method takes advantage on the fact that different substrates have different entry points. The same procedure is used for endogenous metabolites, except that all intracellular metabolites were assigned as fully labelled, and all input substrates as unlabelled. Calculations were based only on the active pool, whereas the stagnant pools were ignored. To generate the percentage value, the total carbon of a substrate in a particular metabolite pool was then divided by the total carbon of that pool. Substrate redistribution estimates provided (Data S1).

Evaluating goodness-of-fit

Figure S3E showed that the residual errors from the best INS and CTRL solutions were not normally distribution. The largest 10 residuals contributed to 20% of the SSR. Problematic data points were flagged (Supplemental Information Data S1). They were mainly mapped to the first timepoint, intermediate masses and extracellular lactate. Potential explanations are that (i) the initial condition defined for modelling differed from the actual, (ii) isobaric interferences causing higher than expect intermediate enrichments (m1 to m5), and (iii) mismatched lactate secretion rates because intracellular and extracellular data were obtained from separate adipocyte batches. Apart from (iii) affecting CTRL lactate efflux, trial removal of these data points did not appear to alter fluxes (results not shown).

Flux difference mappings

Monte-Carlo resampling yielded 50 solutions per condition. To subtract effects of media exchange, flux differences were calculated by subtracting CTRL fluxes from INS fluxes (INS – CTRL). To ensure adequate and unbiased representation, every solution from CTRL and INS is paired exactly 10 times chosen at random but without repeats. Flux differences are thus calculated from 500 unique pairs of CTRL and INS solutions. There is a total of 81 flux parameters: 66 original reactions and 15 net fluxes. This gives a total 40500 observations (81×50×10).

Clustering by CP coordinates

B-splines show strong convex hull properties; it is contained within the control polygon with CPs representing the Cartesian coordinates of the edges. Thus, the clustering of temporal flux differences can be accomplished using coordinates of the CPs of INS – CTRL fluxes. Effectively, clustering is performed on the control polygon of the temporal flux difference, which still captures the dynamics of the flux trajectory.

The addition and subtraction polynomial B-splines of the same order and number of internal knots can be performed on the CPs to yield the same output as performed directly on the B-splines. The CPs' x-coordinates must be aligned before the corresponding CPs' in the y-coordinates are added or subtracted. Knot insertion algorithm is used to align knots of two B-splines with different knot sequence. Knot insertion alters knot sequence and CP values without changing the B-spline.

CTRL and INS temporal fluxes were constructed using O3K1 B-splines; it has one internal knot. Performing INS – CTRL on a given reaction produces a B-spline with 2 internal knots derived from CTRL's and INS's knot, and one additional CP. The procedure involves inserting the conjugate knot in CTRL and INS, revising the CPs to reflect the new knot sequence, and finally producing the y-coordinates by taking the difference in CPs. CPs x-coordinates are calculated using the new knot sequence. This produces the coordinates of the CPs for INS – CTRL fluxes.

Clustering was performing using the resulting CP coordinates as variables. MATLAB function *kmeans* was used, with 10 replicates performed to search for lower local minima. Distance metric was based on the squared Euclidean distance. The number of optimum clusters was determined using elbow and silhouette plots.

Eight clusters captured different temporal dynamics (shape of curve) and were assigned to different colours (Figure 5A). #1 showed small steady state change. #2 and #7 showed rapid initial transient followed by sustained steady state. #3, #4, #5 and #6 showed a more gradual ramp towards steady state. #2 and #3 showed sustained steady state, but #5 showed a downturn, and #6 showed a late surge. #8 showed a decrease, but this is associated with the reversibility of lactate dehydrogenase.

Heat map (Figure S5A) was generated with the help of MATLAB function *dendrogram* to sort row and columns based on their dissimilarity matrices.

## Supplemental Reference


Fazakerley, D.J., Naghiloo, S., Chaudhuri, R., Koumanov, F., Burchfield, J.G., Thomas, K.C., Krycer, J.R., Prior, M.J., Parker, B.L., Murrow, B.A., et al. (2015). Proteomic Analysis of GLUT4 Storage Vesicles Reveals Tumor Suppressor Candidate 5 (TUSC5) as a Novel Regulator of Insulin Action in Adipocytes. J. Biol. Chem. *290*, 23528-23542.

Folch , J., Lees, M., and Sloane Stanley, G.H. (1957). A simple method for the isolation and purification of total lipides from animal tissues. J. Biol. Chem. *226*, 497-509.

Hirayama, A., Kami, K., Sugimoto, M., Sugawara, M., Toki, N., Onozuka, H., Kinoshita, T., Saito, N., Ochiai, A., Tomita, M., et al. (2009). Quantitative metabolome profiling of colon and stomach cancer microenvironment by capillary electrophoresis time-of-flight mass spectrometry. Cancer Res. *69*, 4918-4925.

Kanehisa, M., Goto, S., Hattori, M., Aoki-Kinoshita, K.F., Itoh, M., Kawashima, S., Katayama, T., Araki, M., and Hirakawa, M. (2006). From genomics to chemical genomics: new developments in KEGG. Nucleic Acids Res. *34*, D354-357.

Klampfl, C.W., and Buchberger, W. (2001). Determination of carbohydrates by capillary electrophoresis with electrospray-mass spectrometric detection. Electrophoresis *22*, 2737-2742.

Krycer, J.R., Diskin, C., Nelson, M.E., Zeng, X.Y., Fazakerley, D.J., and James, D.E. (2018). A gas trapping method for high-throughput metabolic experiments. Biotechniques *64*, 27-29.

Prabhu, A.V., Krycer, J.R., and Brown, A.J. (2013). Overexpression of a key regulator of lipid homeostasis, Scap, promotes respiration in prostate cancer cells. FEBS Lett. *587*, 983-988.

Soga, T., and Heiger, D.N. (2000). Amino acid analysis by capillary electrophoresis electrospray ionization mass spectrometry. Anal. Chem. *72*, 1236-1241.

Soga, T., Igarashi, K., Ito, C., Mizobuchi, K., Zimmermann, H.P., and Tomita, M. (2009). Metabolomic profiling of anionic metabolites by capillary electrophoresis mass spectrometry. Anal. Chem. *81*, 6165-6174.

Stansbie, D., Brownsey, R.W., Crettaz, M., and Denton, R.M. (1976). Acute effects in vivo of anti-insulin serum on rates of fatty acid synthesis and activities of acetyl-coenzyme A carboxylase and pyruvate dehydrogenase in liver and epididymal adipose tissue of fed rats. Biochem. J. *160*, 413-416.

Sugimoto, M., Wong, D.T., Hirayama, A., Soga, T., and Tomita, M. (2010). Capillary electrophoresis mass spectrometry-based saliva metabolomics identified oral, breast and pancreatic cancer-specific profiles. Metabolomics *6*, 78-95.

Suthers, P.F., Burgard, A.P., Dasika, M.S., Nowroozi, F., Van Dien, S., Keasling, J.D., and Maranas, C.D. (2007). Metabolic flux elucidation for large-scale models using $^{13}C$ labeled isotopes. Metab. Eng. *9*, 387-405.

Thompson, A.L., Lim-Fraser, M.Y., Kraegen, E.W., and Cooney, G.J. (2000). Effects of individual fatty acids on glucose uptake and glycogen synthesis in soleus muscle in vitro. Am. J. Physiol. Endocrinol. Metab. *279*, E577-584.

Van Handel, E. (1965). Estimation of glycogen in small amounts of tissue. Anal. Biochem. *11*, 256-265